Wang, D., Guo, J. (2017): Late Archean high-pressure pelitic granulites in the Yinshan Block, North China Craton. - *Precambrian Research*, *303*, pp. 251—267.

DOI: http://doi.org/10.1016/j.precamres.2017.03.027

Precambrian Research xxx (2017) xxx–xxx

Contents lists available at ScienceDirect

Precambrian Research

journal homepage: www.elsevier.com/locate/precamres

Late Archean high-pressure pelitic granulites in the Yinshan Block, North China Craton

Dan Wang [a,b,*], Jinghui Guo [a,c]

[a] State Key Laboratory of Lithospheric Evolution, Institute of Geology and Geophysics, Chinese Academy of Sciences, Beijing 100029, China
[b] GFZ German Research Centre for Geosciences, Telegrafenberg, D-14473 Potsdam, Germany
[c] College of Earth Science, The Graduate School, Chinese Academy of Sciences, China

ARTICLE INFO

Article history:
Received 29 November 2016
Revised 17 March 2017
Accepted 21 March 2017
Available online xxxx

Keywords:
Late Archean
High-pressure pelitic granulites
P–T pseudosection
Yinshan Block
North China Craton

ABSTRACT

Ancient high-pressure metamorphism provides constraints for the understanding of Archean tectonic processes. Archean high-pressure metamorphic rocks, however, are rarely preserved in old cratons. Here, we report the newly discovered Archean high-pressure metapelites in the Yinshan Block of the North China Craton. The peak metamorphic stage (M2) is represented by kyanite, garnet, plagioclase, K-feldspar, quartz, rutile and melt. Kyanite was replaced by sillimanite during post-peak (M3) decompression process. Phase equilibria modelling in the MnNCKFMASHT system indicates nearly isothermal decompression with peak conditions of 840–870 °C and >14–11 kbar. Secondary ion mass spectrometry (SIMS) zircon U–Pb dating of leucosome (13XWL35) and monazite U–Pb dating of kyanite-garnet-bearing metapelite (13XWL22) yield similar ages of ~2520 Ma, which represent the crystallization age of granulite-facies melt. The high-pressure metapelites are enriched in Na_2O (1.8–3.0 wt.%), MgO (3.4–5.7 wt.%), Cr (245–421 ppm) and Ni (21.0–91.9 ppm) contents, suggesting that volcanic rocks are probably the main sedimentary provenance. High $\delta^{18}O$(WR) values (up to 12.4‰) and zircon oxygen isotopes (av. 11.4‰) of the metasediment source indicate they have undergone low-temperature alteration. The pressure-temperature-time constraints of this study provide a rare record indicating that surficial sediments have been buried to a depth of >40 km at ca. 2520 Ma in the Yinshan Block. Such crustal thickening, combined with available synchronous magmatism suggests that high-pressure metamorphism was triggered in a late Archean deep arc setting in the Yinshan Block of the North China Craton.

1. Introduction

Archean high-pressure (HP) rocks have been recognized in the Barberton greenstone belt of South Africa (Moyen et al., 2006), southern India (Anderson et al., 2012) and the Fennoscandian shield of Russia (Li et al., 2015; Mints et al., 2010). HP granulites with clockwise P–T paths have originated in thickened crust involving subduction and continent–continent collision (Brown, 2007; Carswell and O'Brien, 1993; Ellis, 1987; Guo et al., 2002; Harley, 1989; Klemd and Bröcker, 1999; Kryza et al., 1996; Thompson and England, 1984; Zhao et al., 2000). Therefore, ancient HP rocks with clockwise P–T paths place constraints on the tectonic modes of the early Earth and the onset of plate tectonics (Brown, 2006, 2007; Condie and Kröner, 2008, 2013; Diener et al., 2005, 2006). HP pelitic granulites are of particular interest, because they represent sediments that were brought to the lower continental crust in an active continental margin or through continent(arc)-continent collision processes (Appel and Schenk, 1998; Anderson et al., 2012). Thus, the sequential metamorphic P–T path of Archean HP pelitic granulites provides critical constraints for the understanding of the tectonic history of ancient continental crust.

The North China Craton (NCC) is one of the oldest Archean continents with trondhjemitic gneiss as old as ~3.8 Ga (Liu et al., 1992; Nutman, 2001; Wang et al., 2015a). The Archean tectonic framework of the NCC is still under debate. Some models interpret the NCC to have amalgamated from at least six micro-blocks along several Neoarchean greenstone belts (Zhai, 2011, 2014; Zhai and Santosh, 2011). Other models interpret the NCC to have grown by successive accretion of microblocks, arcs, oceanic plateaus, with progressively younger material added in the west to northwest between 2.5 and 1.85 Ga (Kusky and Li, 2003; Kusky et al., 2007, 2016; Kusky, 2011). These contrasting models mainly base on

* Corresponding author at: State Key Laboratory of Lithospheric Evolution, Institute of Geology and Geophysics, Chinese Academy of Sciences, Beijing 100029, China.
E-mail address: wangdan@gfz-potsdam.de (D. Wang).

http://dx.doi.org/10.1016/j.precamres.2017.03.027
0301-9268/

geological mapping in combination with geophysical and geochronological data (Geng et al., 2012; Jahn et al., 1990; Jahn et al., 2008; Wan et al., 2005, 2011; Wu et al., 2005; Zhai et al., 2007). Metamorphic studies of the Archean boundaries within the NCC, however, are largely lacking, even though the metamorphic history of the boundaries and in particular of those with a HP metamorphic history provide constraints to distinguish among competing explanations.

We present data from a detailed geological field study, P–T modelling, zircon and monazite geochronology, geochemistry and oxygen isotopes from a newly discovered occurrence of the Archean HP pelitic granulites in the Yinshan Block of the NCC. Our aims are (1) to define the late Archean (~2520 Ma) HP granulite-facies metamorphic P–T paths; (2) to investigate the nature source of sediments; and (3) to assess the possible tectonic environment triggered by Archean crustal thickening processes in the NCC.

2. Geological setting and sampling

2.1. Tectonic subdivision of the North China Craton

The NCC (Fig. 1a–c) with ~3.80 Ga trondhjemitic gneiss is one of the oldest cratons in the world (Liu et al., 1992; Song et al., 1996; Wan et al., 2005; Wang et al., 2015a). It has experienced complex subduction-collision-continental break-up evolutional history during Archean to Paleoproterozoic (Kusky et al., 2016; Santosh, 2010; Zhai et al., 2000; Zhao et al., 1998). Because of the preserved Archean rocks in the NCC were metamorphosed under high-grade metamorphic conditions and are strongly deformed (Polat et al., 2006; Wang et al., 2013; Zhao et al., 2001, 2010), it is not easy to recognize the suture zones and tectonic evolution history of the NCC. Different tectonic subdivision and timing of amalgamation of the NCC, have been proposed (Fig. 1a–c, Zhai et al., 2000; Zhao et al., 2012; Kusky et al., 2016).

There are three models for the formation of the NCC. The first model is that the NCC was divided into six micro-continental blocks (Jiaoliao, Qinhuai, Xuchang, Fuping, Jining, Yinshan and Alxa Blocks) that were merged into the NCC around ~2.7–2.5 Ga (Fig. 1a, Zhai et al., 2010; Zhai, 2011, 2014; Zhai and Santosh, 2011, 2013). The ~2.7 Ga and ~2.5 Ga Neoarchean greenstone belts probably represent the arc-continent collisional sutures (Fig. 1a, Zhai and Santosh, 2011). In the second model, the NCC includes two distinct Archean to Paleoproterozoic blocks, i.e., the Eastern Block and Western Block, along the ~1.9–1.8 Ga collisional trans-North China Orogen (Fig. 1b, e.g. Guo et al., 2001, 2005; Zhao et al., 1998, 2002, 2005, 2007, 2008; Wei et al., 2014). The Western Block formed by collision of the Ordos Block and the Yinshan Block along the east-west-trending Khondalite Belt at ~1.95 Ga (Fig. 1b, Guo et al., 2012; Li et al., 2011; Santosh, 2010; Wang et al., 2011; Yin et al., 2009, 2011, 2014; Zhao et al., 2005). The Ordos Block is mostly covered by Mesozoic-Cenozoic sedimentary rocks (Wan et al., 2013), and is supposed to be an Archean or Paleoproterozoic terrane (e.g. Gong et al., 2014; Hu et al., 2014; Tang et al., 2014; Zhang et al., 2015). A third model considers that the eastern unit of the NCC consists of several different small blocks assembled between 2.6 and 2.7 Ga. Subsequently, a >1300 km long arc and accretionary prism collided with the margin of the Eastern Block at 2.5 Ga (Fig. 1c). The NCC grew by accretion of ~2.4 Ga island arcs,~2.3 Ga oceanic plateaus and 1.9–1.8 Ga ribbon microcontinents from the Eastern Block to the west (Fig. 1c, Kusky et al., 2007, 2016; Kusky, 2011).

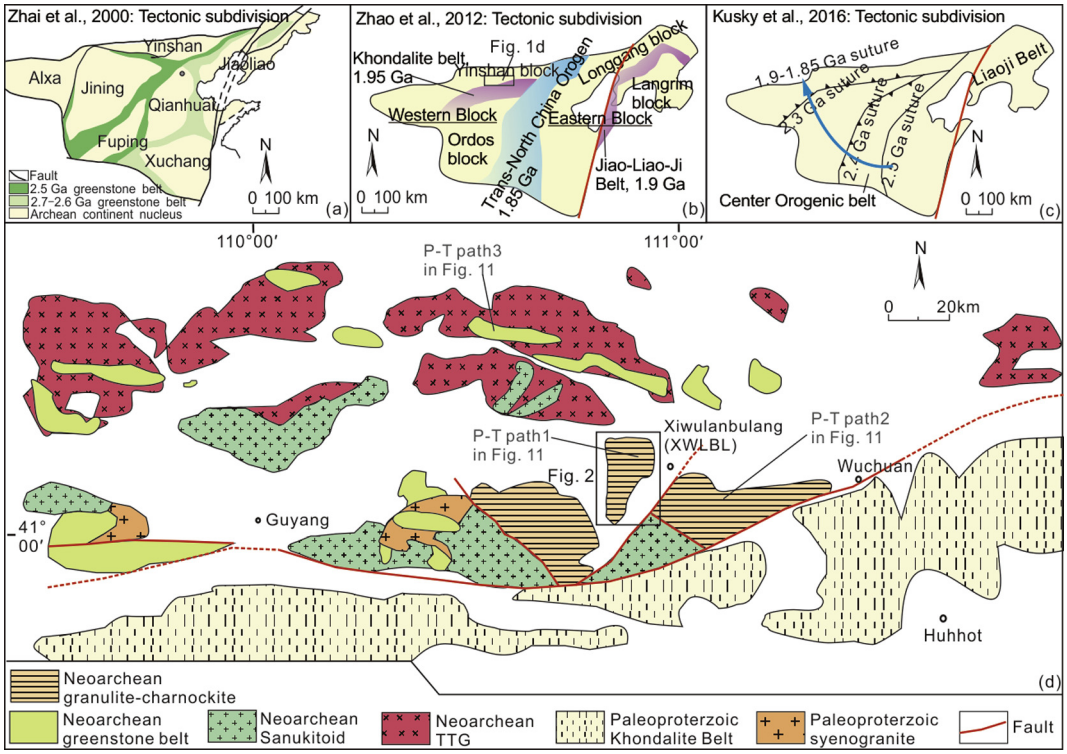

Fig. 1. (a–c) Models for the tectonic subdivision of the North China Craton (NCC). (a) Six micro-continental blocks were merged into the NCC at ~2.7–2.5 Ga (Zhai et al., 2000). (b) the NCC was divided into two Archean Blocks (Eastern and Western Blocks) along three ~1.9–1.8 Ga collisional orogenic belts (Zhao et al., 2012). (c) There is a >1300 km-long arc and accretionary prism collided with the margin of the Eastern Block at ~2.5 Ga in the NCC (Kusky et al., 2016). Oceanic plateaus, microcontinents, and accretionary prisms are younger and westward accretion by 2.4 Ga, 2.3 Ga, 1.9–1.8 Ga in the NCC. (d) Simplified geological map of the Yinshan Block in the Guyang and Wuchuan areas (modified after Ma et al., 2013b).

Please cite this article in press as: Wang, D., Guo, J. Late Archean high-pressure pelitic granulites in the Yinshan Block, North China Craton. Precambrian Res. (2017), http://dx.doi.org/10.1016/j.precamres.2017.03.027

2.2. Geological background of Xiwulanbulang area

The Yinshan Block (Fig. 1b) is juxtaposed against the Khondalite Belt to the north along the Jiuguan-Xiashihao fault. The Paleoproterzoic Khondalite Belt dominantly includes metasedimentary rocks, and includes minor tonalite–trondhjemite–granodiorite (TTG) gneisses, mafic granulites, syntectonic charnockites and S-type granites (e.g. Dong et al., 2012a; Jiao et al., 2013a,b; Peng et al., 2011, 2012). These rocks underwent upper amphibolite- to granulite-facies metamorphism at ca. 1.95–1.92 Ga (Lu et al., 1992; Lu and Jin, 1993; Wan et al., 2006, 2009; Xia et al., 2006a, b; Yin et al., 2009, 2011). In contrast, the Yinshan Block contains abundant Archean rock units, including ~2.5 Ga Guyang greenstones, ~2.6 Ga mafic-ultramafic complex, ~2.7 and ~2.5 Ga TTG gneisses, ~2.56 and ~2.52 Ga high-Mg diorites, ~2.52 Ga granulites, charnockites and late Archean meta-sedimentary rocks (Fig. 1d, Chen, 2007; Jian et al., 2005, 2012; Ma et al., 2013a,b; Zhang et al., 2014; Wang et al., 2015b). Two-pyroxene granulites and plagioclase amphibolites record ~2.5 Ga isobaric cooling P–T paths (Jin et al., 1991). Metamorphic zircons from the TTG, greenstones and meta-sedimentary rocks give a metamorphic age of ~2.5 Ga (Wang et al., 2015b). The ~1.9 Ga high-temperature and high-pressure metamorphism in the Khondalite Belt has weak influence on the Archean rocks of the Yinshan Block.

The Xiwulanbulang (XWLBL) area is part of high-grade metamorphic Archean terrane in the Yinshan Block. The preserved Archean rock associations at the XWLBL area include ~70–75% charnockites and gneissic granites, ~20% mafic to intermediate intrusive rocks, and ~5–10% meta-sedimentary rocks (Fig. 2, Xu et al., 2011; Dong et al., 2012b). All these rocks have been variably affected by ~2.5 Ga regional amphibolite- to granulite-facies metamorphism (Dong, 2009; Wang et al., 2015b). Geological field work shows that meta-sedimentary rocks occur as fragments within ca. 2.56–2.52 Ga TTG rocks.

The garnet-kyanite-bearing two feldspar gneiss (13XWL22) is strongly deformed, and most foliations in the rocks have dips towards the NNW (330°, Fig. 3a). The associated undeformed leucosome (14XWL35) cut through the NNW foliations of metapelitic rocks (Fig. 3b), presenting that the melt crystallized slightly later than peak metamorphism and deformation. Kyanite in the metapelite forms fine-grained elongated metaphenocryst, while kyanite in the leucosome forms coarse-grained metaphenocryst (Fig. 3c–d). The meta-sedimentary unit coexists with mafic and ultramafic complex, and it was intruded by pyroxene hornblendite (Fig. 3e). Except garnet-kyanite gneisses, the metasedimentary rocks also include garnet quartzite (Fig. 3f) and biotite-garnet plagioclase gneiss.

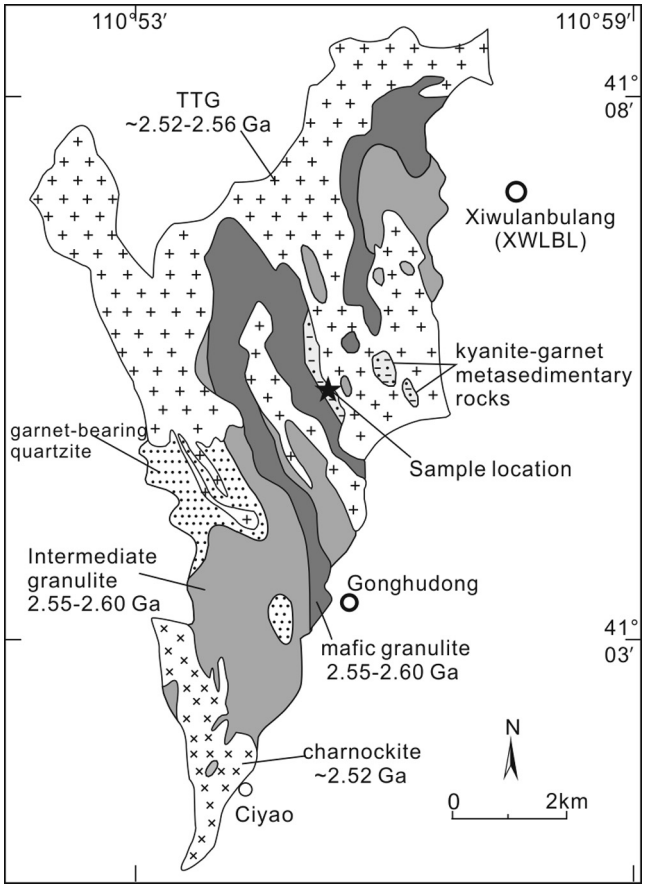

Fig. 2. Geological map of the Xiwulanbulang (XWLBL) area in the Yinshan Block. Modified after Dong (2009).

3. Analytical methods

3.1. Mineralogical major element analysis

Major element compositions of rock-forming minerals were determined on a JEOL JXA-8100 EMP at the Institute of Geology and Geophysics, Chinese Academy of Sciences (IGGCAS). Mineral major elements were obtained using a JEOL JXA-8100 electron microprobe (EMP) with 15 kV accelerating voltage, 20 nA beam current and 3 or 5 μm spot size. Counting times were 20 s on peaks and 10 s on each background. Relative standard deviations of the analyses of standard minerals are better than ±1%.

3.2. Whole rocks major and trace elements

Whole rock major elements were determined in the State Key Laboratory of Geological Processes and Mineral Resources, China University of Geosciences, Wuhan. Major elements were analyzed by on-fused glass discs using a XRF-1800 Sequential X-ray Fluorescence Spectrometer from Shimadzu. The analytical uncertainties, monitored by replicates and two standards (syenite GSR-7 and basalt GSR-3), are less than 1%. The loss-on-ignition (LOI) was measured on dried rock powder by heating in a pre-heated corundum crucible to 1000 °C for 90 min and recorded the percentage weight loss.

Trace elements were analyzed using an Agilent 7500e inductively coupled plasma mass spectrometry (ICP–MS) at the Key Laboratory of Orogenic Belts and Crustal Evolution, Peking University. The international standards GSR-1 (granite), GSR-3(basalt), GSR-2 (andesite) were used for analytical quality control. The relative analytical uncertainties for all elements are <3%. The detailed analytical methods and procedures were described by Liu et al. (2004).

3.3. Zircon and monazite SIMS U–Pb dating

Zircon and monazite were separated from crushed rock samples using conventional density and magnetic techniques. Unknown zircon and monazite samples were mounted in epoxy mounts with zircon standards Penglai, Qinghu and Plesovice, and monazite standard 44069, respectively, and then polished to expose crystal interior for analysis. All samples were documented with transmitted and reflected light micrographs, cathodoluminescence (CL) images (for zircon), and back-scattered images (BSE for monazite) to reveal their internal structures. CL imaging was carried out using a Nova Nano 450 scanning electron microscope (SEM) coupled with a Gatan MonoCL4 Cathodoluminescence system at the IGGCAS. BSE

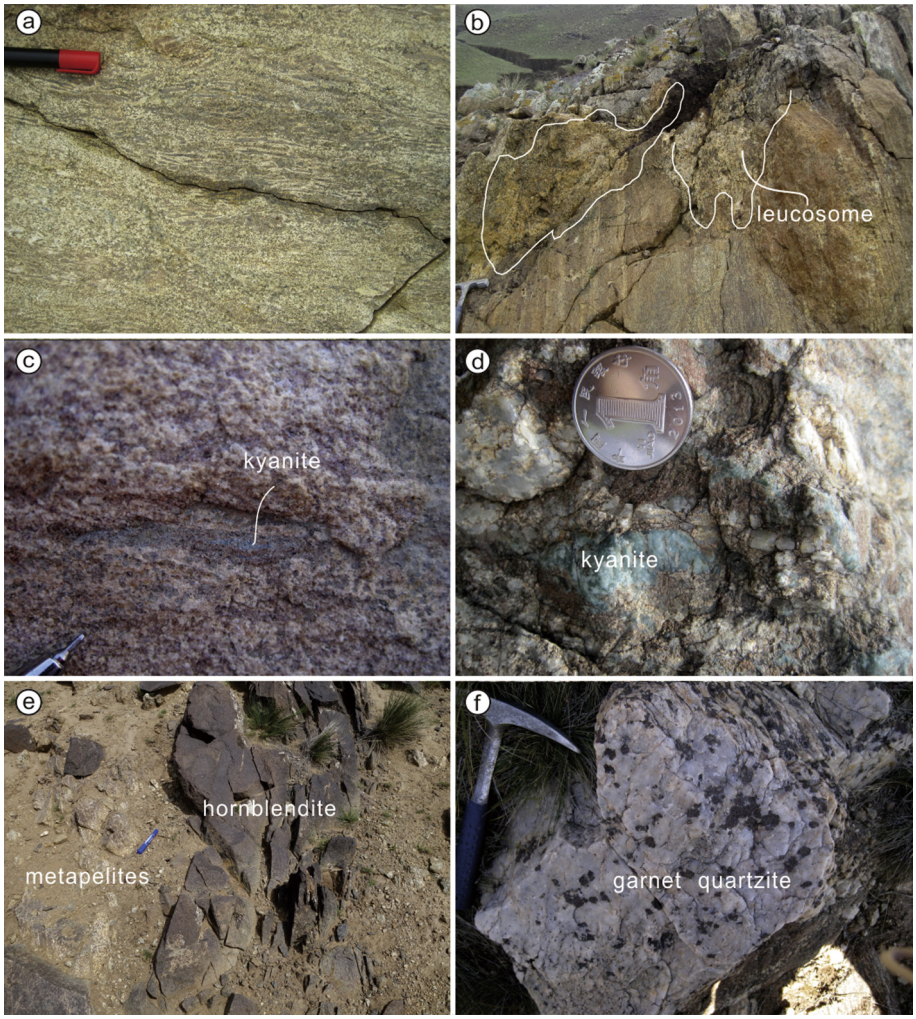

Fig. 3. Field photographs of the XWLBL metapelites locality. (a) NNW foliation of kyanite-garnet-bearing gneiss; (b) leucosome cut through the foliation of metapelites; (c–d) fine-grained or coarse-grained kyanite crystals were both developed in the hand specimen; (e) hornblendite veins intruded the metapelites; (f) co-existed garnet quartzite with kyanite-garnet-bearing gneiss.

images were taken using a CAMECA SX Five FE at the IGGCAS, with a beam current of 40 nA.

Measurements of zircon U, Th and Pb isotopes were conducted using a Cameca IMS-1280 SIMS at the IGGCAS. U–Th–Pb ratios and absolute abundances were determined relative to the Qinghu (Li et al., 2009). The analyses of unknown samples were interspersed with Qinghu. Data processing procedures were similar to those described by Li et al. (2009). During the analysis, the O^{2-} primary ion beam was accelerated at 13 kV, with an intensity of ca. 8 nA and a beam size of 20 × 30 μm. A long-term uncertainty of 1.5% (1 RSD) for $^{206}Pb/^{238}U$ measurements was propagated to the unknowns (Li et al., 2010c), although error of the measured $^{206}Pb/^{238}U$ in a single session was generally around 1% (1 RSD) or less. Measured compositions were corrected for common Pb using non-radiogenic ^{204}Pb. Corrections were sufficiently small to be insensitive to the choice of common Pb composition, and an average of present-day crustal composition (Stacey and Kramers, 1975) was used for common Pb, assuming that common Pb was largely surface contamination introduced during sample preparation.

U–Th–Pb isotopic analyses on monazite were conducted using a Cameca IMS-1280HR SIMS at the IGGCAS. U–Th–Pb ratios and absolute abundances were determined relative to the monazite standard 44069 (Aleinikoff et al., 2006), analyses of which were interspersed with those of unknown grains. The O^{2-} primary ion beam was accelerated at 13 kV, with an intensity of ca. 2–3 nA and a beam size of 20 × 30 μm. A ^{207}Pb-based common Pb and ^{230}Th correction methods were used (Williams, 1998; Li et al., 2013) considering the obvious isobaric interference of $^{232}Th^{144}Nd^{16}O^{2+}$ on ^{204}Pb. Detail analytical procedure is referred to Li et al. (2013).

Uncertainties on individual U–Th–Pb analyses were reported at a 1SD level, and mean ages of pooled U/Pb (and Pb/Pb) analyses were quoted with 95% confidence interval. Data reduction was carried out using Isoplot/Ex v. 3.71 (Ludwig, 2009). Average U–Pb ages are quoted at 95% confidence level.

3.4. Zircon SIMS O isotope measurement

Zircon oxygen isotopes were also measured using a Cameca IMS-1280 SIMS, with analytical procedures similar to those described by Li et al. (2010a). The Cs^+ primary ion beam was accelerated at 10 kV with an intensity of ca. 2 nA. The beam was about 10 μm in diameter. The normal-incidence electron flood gun was used to compensate for sample charging during analysis with homogeneous electron density over a 100 μm oval area. The intensity of ^{16}O was typically 1×10^9 cps. Oxygen isotopes were measured in multi-collector mode using two off-axis Faraday cups. Uncertainties on individual analyses were reported at 1σ level.

Please cite this article in press as: Wang, D., Guo, J. Late Archean high-pressure pelitic granulites in the Yinshan Block, North China Craton. Precambrian Res. (2017), http://dx.doi.org/10.1016/j.precamres.2017.03.027

Measured $^{18}O/^{16}O$ was normalized to Vienna Standard Mean Ocean Water (VSMOW, $^{18}O/^{16}O = 0.0020052$) by the following equation: $\delta^{18}O_M = [(^{18}O/^{16}O)_M/0.0020052 - 1] \times 1000‰$. With low noise on the two FC amplifiers, the internal precision of a single analysis was generally better than 0.2‰ (1SE). The external precision, measured by the reproducibility of repeated analyses of Penglai standard, is 0.40‰ (2SD). The instrumental mass fractionation factor (IMF) was corrected using zircon standard Penglai with $\delta^{18}O_{VSMOW} = 5.3‰$ ($IMF = \delta^{18}O_{M(Penglai)} - 5.3‰$, $\delta^{18}O_{Sample} = -\delta^{18}O_M + IMF$, Li et al., 2010b).

3.5. Whole-rock oxygen isotopes

Whole-rock O isotope ratios [as $\delta^{18}O$ values relative to Standard Mean Ocean Water (SMOW)] were determined using a Finnigan MAT-252 mass spectrometer at the IGGCAS. CO_2 produced from oxygen liberated by overnight reaction of whole-rock powders with BrF_5 at 550 °C and converted into CO_2 by reaction with hot graphite. The analytical precision is 0.2‰.

4. Petrography and mineral chemistry

The kyanite-garnet-bearing two feldspar gneisses (13XWL22) contain 0.4–3.0 mm subhedral porphyroblastic garnet, ≤2 mm bladed porphyroblastic kyanite, <0.5 mm fibrous/tabular porphyroblastic sillimanite, fine-grained platy to equant plagioclase, K-feldspar and quartz grains (0.2–2.5 mm), 0.2 mm-long biotite, rare fine-grained rutile (≤1 mm) and prismatic graphite (≤0.5 mm) with minor zircon, apatite, ilmenite and monazite (Fig. 4a–h). Sillimanite and kynite were distinguished by Laser Raman analysis (Appendix Fig. A). Cores of most garnet porphyroblasts contain abundant mineral inclusions of quartz, plagioclase and biotite (Fig. 4c–e). Garnet rims contain significantly fewer inclusions than the cores, most of which are rutile and K-feldspar with minor kyanite (Fig. 4e). The representative prograde assemblage (M1) consists of kyanite, garnet, biotite, plagioclase, quartz and rutile. Biotite only occurs within the garnet porphyroblast, and is absent in the matrix (Fig. 4c–d). The representative mineral assemblage of the peak metamorphic stage (M2) is coarse-grained kyanite, garnet, plagioclase, K-feldspar, quartz, rutile and melt (Fig. 4f). Small sillimanite crystals replaced large bladed kyanite that is in contact with garnet (Fig. 4b, f and g). Therefore, the post-peak assemblage (M3) is interpreted to be sillimanite, garnet, plagioclase, quartz, ilmenite and melt. Representative mineral analyses of garnet, feldspar and biotite are presented in Tables 1–3.

Garnet porphyroblasts are essentially almandine (X_{alm}, 52–54%) and pyrope (X_{prp}, 42–44%), with minor grossular (X_{grs}, 2.9–4.2%) and spessartine (X_{sps}, 0.5–0.7%) components (Fig. 5a–f). The X_{Fe} value ($X_{Fe} = 100 \times Fe/(Mg + Fe)$) of garnet falls in the small range of 54–55. Garnet mostly shows flat major element zoning from core to near the rim (Line A–A′ and B–B′, Fig. 5a and b). At the garnet rims that surrounded by plagioclase, X_{grs} slightly increases, while X_{prp} slightly decreases (Fig. 5d–f) (see Appendix Fig. B).

Biotite only occurs as inclusions in the garnet with high X_{Mg} values of 0.65–0.72. The TiO_2 contents are variable in the range of 2.96–5.44 wt.% and Al^{IV} is about 1.0–1.1. Individual biotite grains are generally homogeneous in compositions. F contents and Cl contents in the biotites are low.

Plagioclase compositions in the matrix are homogeneous with An ($An = Ca/(Ca + Na + K) \times 100\%$) contents in the range of 16–23 mol%, which is classified as oligoclase. Average contents of CaO and Na_2O of plagioclase are 4.11 wt.% and 8.68 wt.%, respectively. K-feldspar have K_2O contents varying of 14.5–14.9 wt.%.

5. Whole-rock major and trace elements

Major and trace elements of the XWLBL kyanite-garnet-bearing two feldspar gneisses are presented in Table 4.

Kyanite-garnet-bearing two feldspar gneisses show variable SiO_2 contents from 59.9 to 67.2 wt.% (Fig. 6a). MgO and CaO contents are high in the range of 3.36–5.68 wt.% and 14.9–19.7 wt.%, respectively, with high Mg# values (43–49) (Fig. 6a–b). Compared with meta-sedimentary rocks from Paleoproterzoic Khondalite belt, the XWLBL meta-sedimentary rocks display high Na_2O contents (1.81–2.98 wt.%), while extremely low K_2O concentrations (0.35–1.80 wt.%) (Fig. 6c and d). TiO_2, MnO and P_2O_5 contents of the XWLBL metapelites are in the range of 0.69–0.95 wt.%, 0.07–0.17 wt.% and 0.02–0.07 wt.%, respectively. The LOI (loss on ignition) is low and varying between 0.35 and 1.80 wt.%.

The XWLBL meta-sedimentary rocks show high Cr and Ni concentrations of 245–421 ppm and 21.0–91.9 ppm, respectively. Sr (81.8–243 ppm) and Ba (129–370 ppm) contents are also high. The XWLBL meta-sedimentary rocks display modestly fractionated LREE patterns with La_N/Sm_N of 3.47–4.41 and flat HREE pattern with Gd_N/Yb_N of 0.66–1.34 on the chondrite-normalized REE diagrams (Fig. 7a). Our samples show slightly positive Eu anomalies ($Eu/Eu^* = 0.9–1.2$). HREE contents are mostly controlled by proportion of garnet in the rocks. All our investigated rocks are characterized by positive Ba, Zr and Hf anomalies and strong depletions of Sr and Ti relative to neighbouring REE (Fig. 7b).

6. Pseudosection modelling

6.1. Methodology

Pseudosections were calculated using THERMOCALC v3.33 (Powell and Holland, 1988) and the thermodynamic dataset tcds55 (Holland and Powell, 1998; updated October 2009). The calculations for kyanite-garnet bearing two feldspar gneiss (13XWL22) were performed in the MnNCKFMASHT ($Mn–Na_2O–CaO–K_2O–FeO–MgO–Al_2O_3–SiO_2–H_2O–TiO_2$) system, which is the most reliable system for metapelites. Fe_2O_3 was neglected because Fe^{3+}-rich phases such as magnetite are absent from the studied sample and the major phases (garnet) do not contain significant amounts of Fe^{3+}.Water activity was set to $a(H_2O) = 1$. Quartz is abundant in the modelled sample and assumed to be in excess. Pseudosection construction considered the following solid-solution models: garnet (g; White et al., 2005), K-feldspar (ksp; Holland and Powell, 2003), plagioclase (pl; Holland and Powell, 2003), muscovite (mu; Coggon and Holland, 2002), Ti-bearing biotite and silicate melt (bi and liq, White et al., 2007), cordierite (cd; Mahar et al., 1997; Holland and Powell, 1998), orthopyroxene (opx, Powell and Holland, 1999), ilmenite (ilm; White et al., 2000). Pure phases include kyanite, sillimanite, rutile, quartz and H_2O.

6.2. P–T pseudosections

For kyanite-garnet-bearing two feldspar gneisses that underwent melt loss, the XRF-based bulk composition was used to model the P–T conditions of melt crystallization or the retrograde evolution (Groppo et al., 2012). A melt-reintegrated bulk composition was used to model prograde metamorphic development of the studied sample (13XWL22, Fig. 8a). Melt composition was calculated based on the average bulk composition of accompanied leucosomes (Appendix Table A). About 30 mol% melt has been reintegrated, as is estimated from the field observations. Saturated water content was used to calculate the melt reintegrated pseudosection. Due to the extremely low K_2O contents of sample 13XWL22 compared with normal metapelites, fields of

Please cite this article in press as: Wang, D., Guo, J. Late Archean high-pressure pelitic granulites in the Yinshan Block, North China Craton. Precambrian Res. (2017), http://dx.doi.org/10.1016/j.precamres.2017.03.027

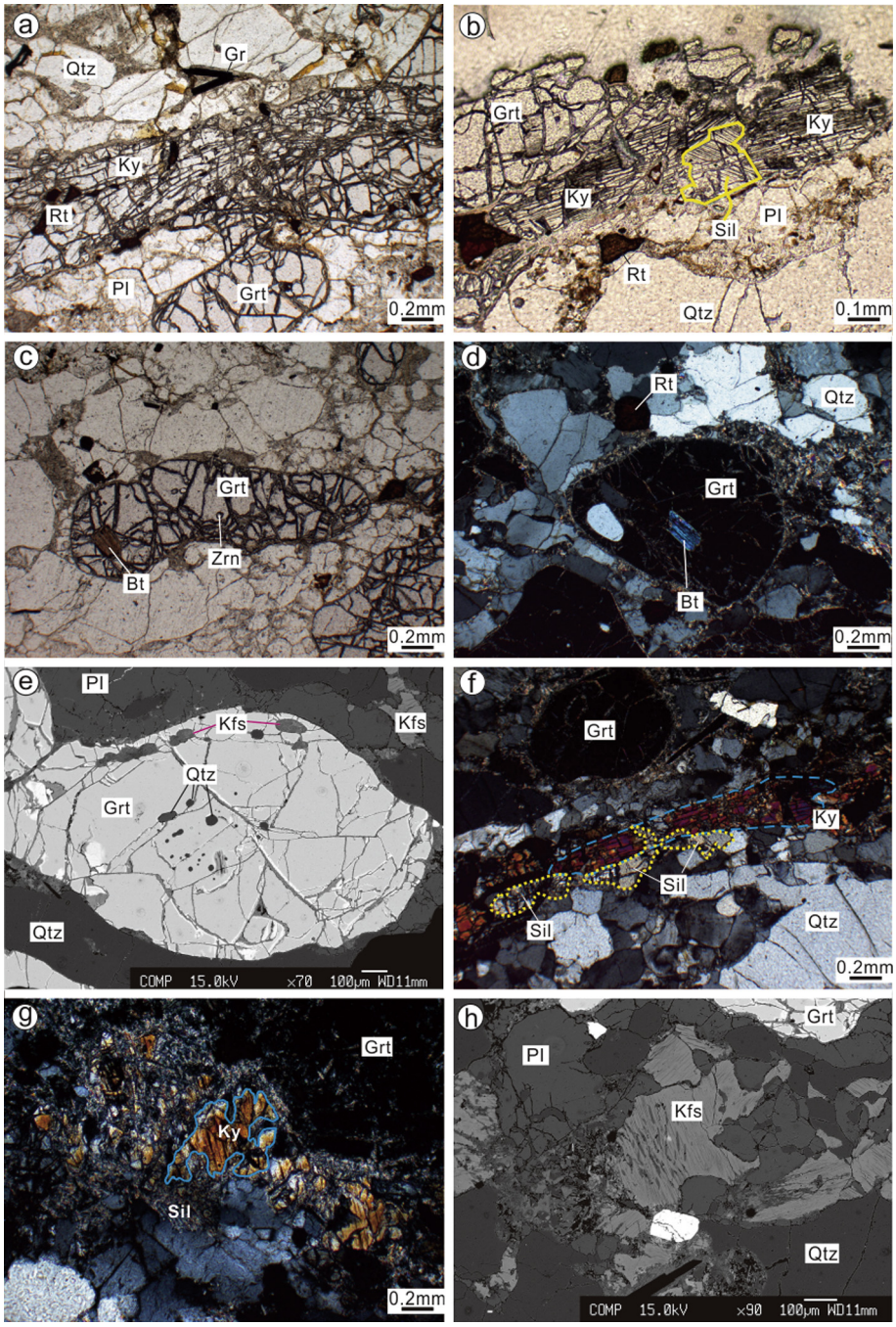

Fig. 4. Photomicrographs showing the mineral assemblages and microtextures of the kyanite-garnet bearing gneiss (13XWL22). (a–c, f) Garnet, kyanite, sillimanite exist as porphyroblasts, while plagioclase, K-feldspar and quartz occur in the matrix; (b, f and g) Small sillimanite crystals replaced large bladed kyanite; (c–d) biotite only occurs as inclusion within the garnet porphyroblast; (e) garnet porphyroblasts contain mineral inclusions of quartz, plagioclase and biotite; (h) K-feldspar with string plagioclase lamellae.

potassium-rich minerals such as K-feldspar, biotite and muscovite in the pseudosection are strongly reduced. Biotite is limited to the medium temperature area, whereas muscovite is restricted to the high-pressure fields. K-feldspar is limited to a narrow field in the pseudosection corresponding to T = 840–870 °C and P >14 kbar. The petrographic evidence suggests that the prograde assemblage (M1), represented by the garnet core and its mineral inclusions of kyanite, biotite, plagioclase, quartz and rutile, should be located in grt–ky–bt–pl–rt–melt field (P = 8–16 kbar, T <830 °C). Peak assemblage (M2), which is represented by kyanite, garnet, plagioclase, K-feldspar, quartz, rutile and melt, defines the grt–ky–kfs–pl–rt–melt field (P >14 kbar, T = 840–870 °C).

The P–T pseudosection shown in Fig. 8b was calculated using the XRF-based bulk composition. The H_2O content of the bulk composition was calculated by combining mineral modes and compositions, which mainly derives from biotite by considering a Ti-H substitution scheme of White et al. (2007). Biotite only occurs as inclusions within garnet, therefore, the calculated water contents is very low (0.28 wt.%). Because of water loss during melt crystallization and migration, the melt-in line in the pseudosection is estimated to be of high temperatures (T >830 °C). In the post-peak decompressional assemblage (M3), sillimanite replaces kyanite (Fig. 4b, f and g). Biotite has not been observed in the matrix. Therefore, the P–T path from M2 to M3 goes from the grt–ky–kf

Please cite this article in press as: Wang, D., Guo, J. Late Archean high-pressure pelitic granulites in the Yinshan Block, North China Craton. Precambrian Res. (2017), http://dx.doi.org/10.1016/j.precamres.2017.03.027

Table 1
Representative chemical compositions of garnet of the kyanite-garnet two feldspar gneiss (13XWL22) from the Yinshan Block.

Sample	81	83	84	85	86	87	88	89	90	92	93	94	95
SiO_2	40.13	41.32	40.13	39.97	39.77	39.82	40.05	39.97	39.89	40.17	39.82	39.90	39.67
TiO_2	0.00	0.03	0.00	0.00	0.04	0.00	0.03	0.01	0.00	0.03	0.00	0.01	0.00
Al_2O_3	22.92	22.94	22.90	22.82	22.93	23.00	22.74	22.96	22.87	22.94	22.91	22.96	22.77
Cr_2O_3	0.12	0.11	0.12	0.12	0.10	0.10	0.09	0.07	0.09	0.12	0.13	0.13	0.16
FeO	25.09	25.25	25.09	25.41	25.28	25.18	25.20	25.14	26.32	25.14	25.08	25.18	25.14
MnO	0.31	0.27	0.31	0.31	0.33	0.33	0.31	0.32	0.28	0.29	0.31	0.25	0.30
MgO	11.55	11.70	11.64	11.68	11.60	11.74	11.48	11.68	11.64	11.70	11.48	11.64	11.37
CaO	1.46	1.17	1.17	1.15	1.21	1.19	1.19	1.16	1.21	1.23	1.26	1.35	1.50
Totals	101.6	102.8	101.5	101.2	101.5	101.5	101.1	101.4	101.1	101.7	101.0	101.4	100.9
Si	2.991	3.034	2.993	2.992	2.971	2.971	3.000	2.984	2.987	2.991	2.986	2.979	2.981
Ti	0.000	0.001	0.000	0.000	0.002	0.000	0.002	0.001	0.000	0.002	0.000	0.001	0.000
Al	2.014	1.986	2.013	2.013	2.019	2.023	2.008	2.021	2.019	2.014	2.026	2.021	2.017
Cr	0.007	0.006	0.007	0.007	0.006	0.006	0.005	0.004	0.005	0.007	0.007	0.008	0.009
Fe^{2+}	1.564	1.551	1.575	1.570	1.553	1.546	1.577	1.565	1.569	1.564	1.573	1.560	1.565
Mn	0.019	0.017	0.019	0.020	0.021	0.021	0.019	0.020	0.018	0.018	0.019	0.016	0.019
Mg	1.283	1.281	1.294	1.303	1.292	1.306	1.281	1.300	1.299	1.298	1.284	1.296	1.272
Ca	0.117	0.092	0.094	0.092	0.097	0.095	0.095	0.093	0.097	0.098	0.101	0.108	0.121
Grs-Ca	3.9	3.1	3.2	3.1	3.3	3.2	3.2	3.1	3.3	3.3	3.4	3.6	4.1
Sps-Mn	0.6	0.6	0.6	0.7	0.7	0.7	0.6	0.7	0.6	0.6	0.6	0.5	0.6
Prp-Mg	43.0	43.6	43.4	43.7	43.6	44.0	43.1	43.7	43.5	43.6	43.1	43.5	42.7
Alm-Fe	52.4	52.7	52.8	52.6	52.4	52.1	53.1	52.6	52.6	52.5	52.8	52.3	52.6
$Fe^{\#}$	55	55	55	55	55	54	55	55	55	55	55	55	55

Table 2
Representative chemical compositions of feldspar of the kyanite-garnet two feldspar gneiss (13XWL22) from the Yinshan Block.

Sample	08PL	09PL	10PL	11PL	38PL	39PL	43PL	44PL	45PL	55PL	73PL	96PL	97PL	99PL	100PL	07KFS	42KFS
SiO_2	62.47	63.92	63.27	63.44	62.94	63.01	63.29	62.94	63.09	64.36	62.38	62.79	63.05	63.42	63.81	64.66	64.23
TiO_2	0.03	0.03	0.04	0.01	0.00	0.00	0.00	0.00	0.03	0.01	0.00	0.00	0.00	0.00	0.01	0.03	0.01
Al_2O_3	22.64	22.63	22.58	22.71	22.84	23.03	22.50	22.80	22.68	22.20	22.92	23.06	23.01	23.00	22.65	18.71	18.53
Fe_2O_3	0.03	0.02	0.01	0.02	0.08	0.11	0.01	0.01	0.05	0.66	0.39	0.24	0.20	0.02	0.02	0.00	0.02
CaO	4.02	4.00	4.08	4.03	4.26	4.41	3.86	3.95	3.99	3.31	4.58	4.23	4.23	4.18	4.05	0.11	0.03
Na_2O	8.61	8.57	8.82	8.79	8.74	8.50	8.85	8.83	8.49	9.27	8.39	8.74	8.55	8.57	8.64	1.09	0.97
K_2O	0.34	0.15	0.17	0.16	0.16	0.13	0.16	0.21	0.17	0.14	0.10	0.13	0.15	0.16	0.11	14.50	14.86
Totals	98.16	99.33	98.98	99.19	99.02	99.21	98.70	98.74	98.51	100.03	98.83	99.21	99.21	99.35	99.32	99.10	98.65
Oxygens	8	8	8	8	8	8	8	8	8	8	8	8	8	8	8	8	8
Si	2.81	2.83	2.82	2.82	2.81	2.80	2.83	2.81	2.82	2.84	2.79	2.80	2.80	2.81	2.83	2.99	2.99
Ti	0.00	0.00	0.00	0.00	0.00	0.00	0.00	0.00	0.00	0.00	0.00	0.00	0.00	0.00	0.00	0.00	0.00
Al	1.20	1.18	1.19	1.19	1.20	1.21	1.18	1.20	1.20	1.15	1.21	1.21	1.21	1.20	1.18	1.02	1.02
Ca	0.19	0.19	0.20	0.19	0.20	0.21	0.18	0.19	0.19	0.16	0.22	0.20	0.20	0.20	0.19	0.01	0.00
Na	0.75	0.74	0.76	0.76	0.76	0.73	0.77	0.77	0.74	0.79	0.73	0.75	0.74	0.74	0.74	0.10	0.09
K	0.02	0.01	0.01	0.01	0.01	0.01	0.01	0.01	0.01	0.01	0.01	0.01	0.01	0.01	0.01	0.86	0.88
Sum	5.0	4.9	5.0	5.0	5.0	5.0	5.0	5.0	5.0	5.0	5.0	5.0	5.0	5.0	5.0	5.0	5.0
An	20	20	20	20	21	22	19	20	20	16	23	21	21	21	20		

Table 3
Chemical compositions of biotite of the kyanite-garnet two feldspar gneiss (13XWL22) from the Yinshan Block.

Sample	32BT	35BT	74BT	78BT	80BT	103BT
SiO_2	37.30	37.47	37.25	35.95	36.48	37.83
TiO_2	2.96	3.20	3.28	5.44	3.96	4.10
Al_2O_3	17.94	16.77	16.80	16.73	16.38	16.88
Cr_2O_3	0.37	0.38	0.39	0.46	0.43	0.45
FeO	10.87	10.60	12.07	11.19	12.65	11.84
MnO	0.00	0.01	0.00	0.00	0.02	0.02
MgO	15.20	14.97	13.93	13.85	12.96	14.57
CaO	0.07	0.04	0.11	0.09	0.05	0.07
Na_2O	0.18	0.13	0.11	0.16	0.14	0.11
K_2O	8.97	9.21	8.97	8.89	9.44	8.96
Totals	93.85	92.78	92.91	92.75	92.52	94.83
Oxygens	11	11	11	11	11	11
Si	2.76	2.80	2.80	2.71	2.78	2.78
Ti	0.17	0.18	0.19	0.31	0.23	0.23
Al	1.56	1.48	1.49	1.49	1.47	1.46
Cr	0.02	0.02	0.02	0.03	0.03	0.03
Fe2	0.67	0.66	0.76	0.71	0.81	0.73
Mn	0.00	0.00	0.00	0.00	0.00	0.00
Mg	1.67	1.67	1.56	1.55	1.47	1.60
Ca	0.01	0.00	0.01	0.01	0.00	0.01
Na	0.03	0.02	0.02	0.02	0.02	0.02
K	0.85	0.88	0.86	0.85	0.92	0.84
Sum	7.7	7.7	7.7	7.7	7.7	7.7

Please cite this article in press as: Wang, D., Guo, J. Late Archean high-pressure pelitic granulites in the Yinshan Block, North China Craton. Precambrian Res. (2017), http://dx.doi.org/10.1016/j.precamres.2017.03.027

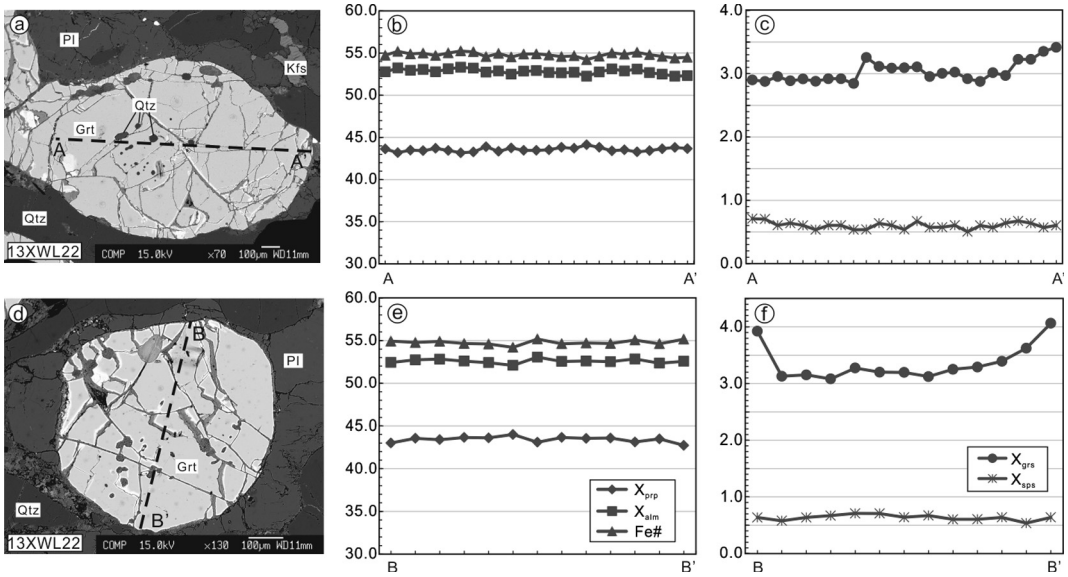

Fig. 5. (a, d) Garnet compositions were analyzed along the lines of A–A′ and B–B′. (b, e) show the chemical variations of pyrope, almandine and Fe# values (Fe# = molar FeO/(FeO + MgO) × 100%) along the lines A–A′ and B–B′. (c, f) show the chemical variations of grossular and spessartine along the lines A–A′ and B–B′.

Table 4
Major and trace elements analysis of XWLBL metapelites from the Yinshan Block.

Sample	14XWL36	13XWL22	14XWL37	14XWL37-1
SiO_2	51.8	59.9	67.2	66.5
TiO_2	0.73	0.77	0.95	0.69
Al_2O_3	19.7	17.2	14.9	15.2
FeOt	11.6	10.9	7.1	7.6
FeO	–	8.35	–	–
MnO	0.17	0.11	0.07	0.09
MgO	5.68	4.16	3.36	3.61
CaO	3.79	1.75	1.45	1.30
Na_2O	2.87	2.98	2.06	1.81
K_2O	1.23	0.76	0.77	0.98
P_2O_5	0.07	0.03	0.03	0.02
LOI	0.35	1.72	1.80	1.70
Total	98.1	100.4	99.6	99.5
Sc	37.9	33.9	26	43.3
V	226	206	187	150
Cr	421	334	293	245
Co	38.5	22.5	30.4	32.9
Ni	91.9	21.0	86.7	75.2
Rb	61.2	19.5	13.7	17.8
Sr	243	87.1	94.6	81.8
Y	20.0	16.4	16.2	29.3
Zr	82.9	107	135	121
Nb	4.68	4.81	5.26	4.82
Ba	370	268	129	154
La	21.9	12.7	12.3	10.7
Ce	48.1	25.4	25.6	21.9
Pr	4.95	2.74	2.68	2.29
Nd	18.4	10.6	10.0	8.42
Sm	3.21	2.36	2.01	1.67
Eu	1.28	0.75	0.88	0.75
Gd	3.27	2.98	2.37	2.67
Tb	0.57	0.51	0.43	0.64
Dy	3.55	3.16	2.85	4.71
Ho	0.70	0.64	0.60	1.09
Er	2.07	1.92	1.76	3.2
Tm	0.32	0.28	0.26	0.52
Yb	2.02	1.85	1.78	3.37
Lu	0.31	0.3	0.26	0.52
Hf	2.19	2.98	3.51	3.13
Ta	0.22	0.56	0.31	0.32
Th	6.31	0.8	0.49	0.29
U	0.30	0.25	0.18	0.14

s–pl–rt–melt field directly into the grt–sill–kfs–pl–rt–melt field (Fig. 8b), which corresponds to isothermal decompression. In the grt–sill–kfs–pl–rt–melt field, garnet (X_{grs} = 0.03–0.04) and plagioclase (minimum An values = 0.16) compositions were used to constrain the retrograde metamorphic P–T conditions 10 and 11 kbar and >850 °C). The X_{grs} and X_{prp} compositions of the garnet were not used to constrain the P–T conditions, because Ca and Mg in garnet have different diffusion rates under the granulite-facies metamorphism (Schwandt et al., 1996).

7. Monazite and zircon U–Pb geochronology

7.1. Monazite U–Pb geochronology of meta-sedimentary rock

Monazite grains from kyanite-garnet–bearing two feldspar gneiss (13XWL22) are euhedral to subhedral with length of 60–150 μm. Homogeneous or weak zoning are shown by BSE imaging (Fig. 9a). Monazites contain zircon, quartz, rutile and K-feldspar inclusions, suggesting that they probably grew during the peak or post-peak stages.

Monazites from sample 13XWL22 yield $^{207}Pb/^{206}Pb$ ages ranging from 2530 to 2515 Ma (Appendix Table B). Twenty grains yield a concordia age of 2519 ± 1 Ma (2SD, MSWD = 0.05), consistent with the weighted mean $^{207}Pb/^{206}Pb$ age of 2521 ± 1 Ma (MSWD = 1.2, n = 20). .

7.2. Zircon U–Pb geochronology of leucosome

Zircon grains from the leucosome (14XWL35) are dark purple, and are subhedral to anhedral. Their lengths range from 100 to 350 μm with length/width ratios of 1.0–1.5. Most zircon crystals show sector zoning, whereas unzoned to weakly zoned zircon is rare (Fig. 9b), suggesting they probably crystallized from granulite-facies partial melt.

Thirty-three U–Pb ages were acquired from 14XWL35 and they give apparent $^{207}Pb/^{206}Pb$ ages of 2548–1927 Ma (Appendix Table C). The U–Pb data define an upper intercept at 2557 ± 38 Ma (MSWD = 1.7). Eleven concordant spots yield a weighted mean $^{207}Pb/^{206}Pb$ age of 2518 ± 10 Ma (MSWD = 0.07, Fig. 9b).

Please cite this article in press as: Wang, D., Guo, J. Late Archean high-pressure pelitic granulites in the Yinshan Block, North China Craton. Precambrian Res. (2017), http://dx.doi.org/10.1016/j.precamres.2017.03.027

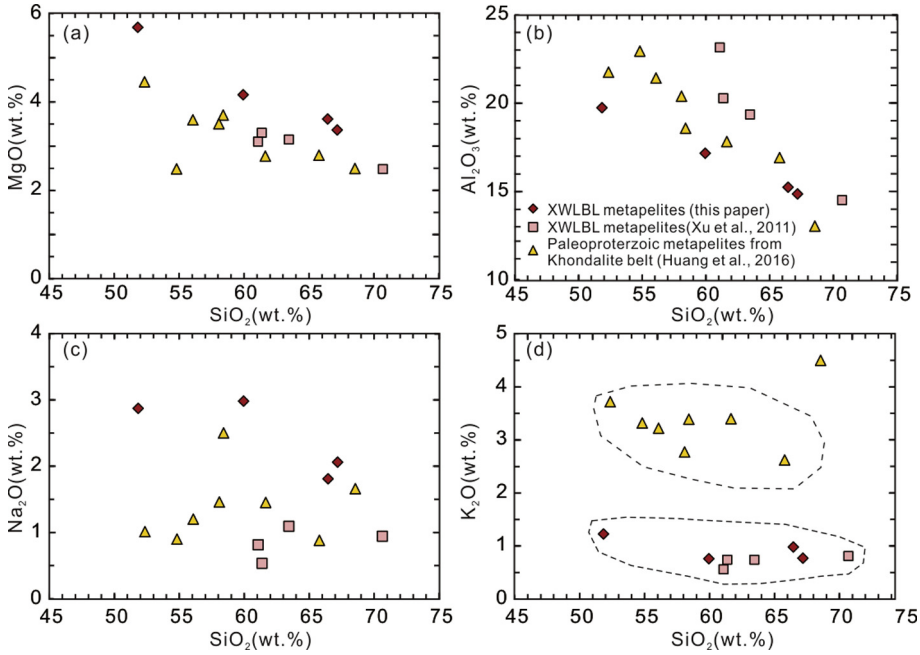

Fig. 6. Whole-rock variations of SiO_2 vs. selected major elements (MgO, Al_2O_3, Na_2O and K_2O) of the XWLBL metapelites in the Yinshan Block; database from Xu et al., 2011 and Huang et al., 2016.

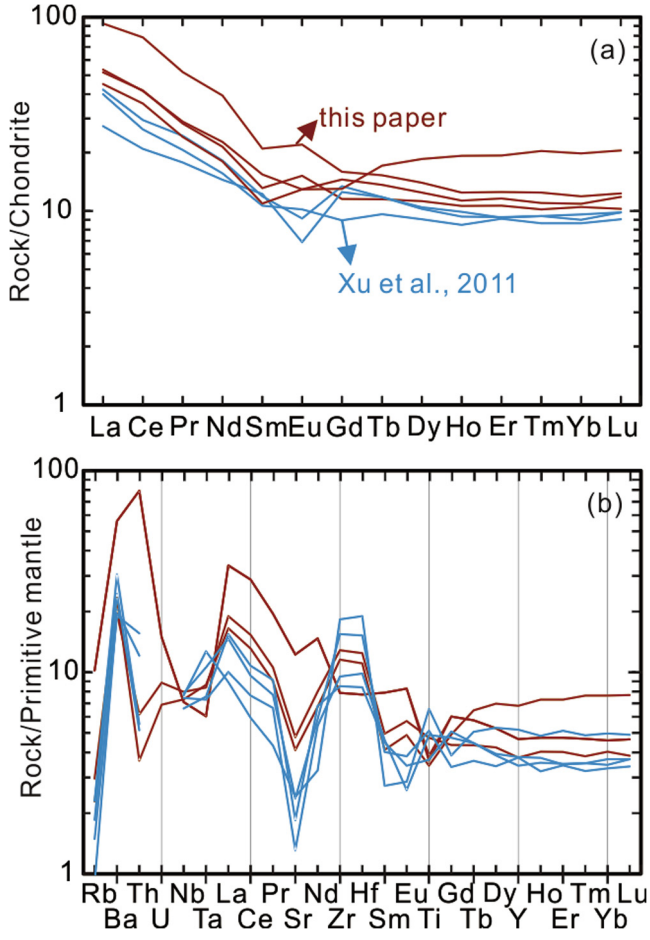

Fig. 7. (a) Chondrite-normalized rare earth element (REE) patterns and (b) Primitive mantle-normalized incompatible element patterns of the XWLBL metapelites in the Yinshan Block. Normalization constants are after McDonough and Sun (1995). Red lines represent data from our study, and blue lines are from Xu et al. (2011).

8. Whole-rock and zircon oxygen isotope

The oxygen isotopes of whole-rock samples (Table 5) and zircons (Appendix Table D) were analyzed. Kyanite-bearing rocks have high $\delta^{18}O$(WR) values in the range of 10.8–12.4‰ (2SD, <0.2‰). Biotite-garnet gneiss show slightly lower $\delta^{18}O$(WR) values of 10.8‰ (2SD, <0.2‰).Zircon U–Pb age data of kyanite-garnet two feldspar gneiss (13XWL22) were reported by Wang et al. (2015b). Most zircon grains show clear core-rim structures (Fig. 10a–d). The cores are detrital magmatic zircons with apparent $^{207}Pb/^{206}Pb$ ages from 2576 Ma to2733 Ma. They give a peak age at ~2610 Ma. These detrital zircon cores have variable $\delta^{18}O$ values ranging from 9.5 to 12.3‰ (Fig. 10e). Thin metamorphic rims show weak or no zoning and yield a weighted mean of 2479 ± 21 Ma. Their $\delta^{18}O$ values are homogeneous with the mean value of 11.4 ± 0.4‰ (Fig. 10e).

9. Discussion

9.1. Metamorphic P–T conditions and evolution

The peak high-pressure granulite-facies assemblage (M2) consists of kyanite, garnet, plagioclase, K-feldspar, quartz, rutile and melt, which constrains the peak P–T conditions at P >14–11 kbar and T = 840–870 °C in the MnNCKFMASHT system (Fig. 8). The post-peak decompression assemblage (M3) is represented by sillimanite replacing kyanite in the matrix (Fig. 4b, f and g). Thus, our modelling results show that the kyanite-garnet gneiss recorded a nearly clockwise-type isothermal decompression P–T path (Fig. 8).

The P–T path reported here is obviously different from the previous anticlockwise P–T paths that were defined based on 'red-eye socket' texture in mafic granulites (Fig. 11, Jin et al., 1991; Liu et al., 1993; Lu and Xu, 1995). Red-eye socket texture, represented by grt + qtz ± cpx replacing previous minerals of plagioclase and pyroxenes, is generally regarded as a post-peak metamorphic reaction, recording a near-isobaric cooling process (Jin et al., 1991; O'Brien et al., 2005). However, some recent studies have pointed out that 'red-eye socket' textures may form in the prograde metamorphic

Please cite this article in press as: Wang, D., Guo, J. Late Archean high-pressure pelitic granulites in the Yinshan Block, North China Craton. Precambrian Res. (2017), http://dx.doi.org/10.1016/j.precamres.2017.03.027

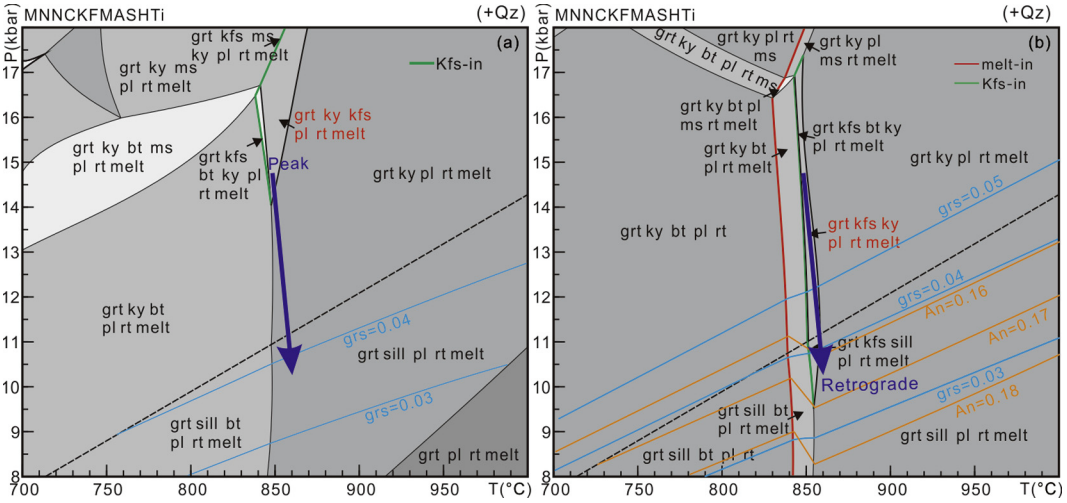

Fig. 8. P–T Pesudosection calculated under MnNCKFMASHT system for kyanite-garnet two feldspar gneiss (Sample 13XWL22) at 8–18 kbar and 700–1000 °C, red characters represent peak mineral assemblage. (a) Pseudosection calculated using the melt-reintegrated bulk composition; (b) Pseudosection calculated using the XRF-based bulk composition.

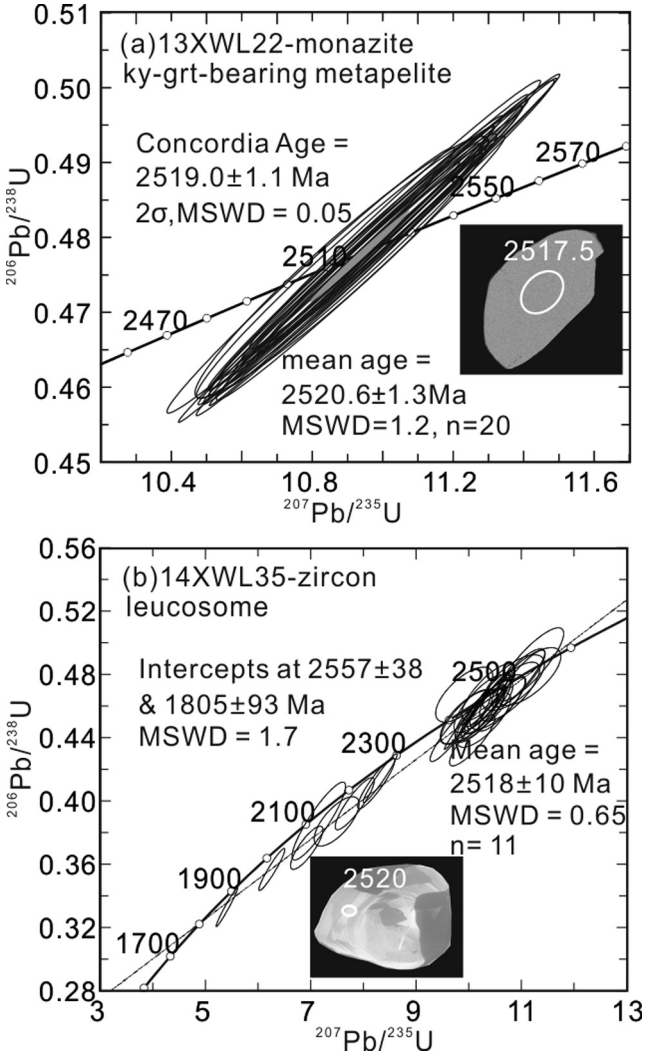

Fig. 9. (a) SIMS monazite U–Pb dating results for the metapelite (13XWL22). Ellipses represent 2SD errors. (b) SIMS zircon U–Pb dating results for the leucosome (14XWL35). Ellipses represent 2SD errors.

stages under fluid-absent conditions not in the post-peak metamorphic stages (Duan et al., 2015; Wei et al., 2014). Therefore, the red-eye socket texture could not represent an anticlockwise P–T path. More evidences, for example prograde mineral assemblage, should be provided when define an anticlockwise P–T path.

On the other hand, if anticlockwise P–T paths exist in the studied area, they are not contradictory to the clockwise P–T path in our study. Clockwise and anticlockwise P–T trajectories from close locations may coexist in a subduction-collision process (Tong et al., 2007). Anticlockwise P–T path requires an additional heat source (such as ultramafic-mafic magmatism, Halpin et al., 2007) that induced the P–T trajectory deviating from a normal thermal gradient. Certainly, not all rocks would be affected by additional heat. Whether an additional heat has influenced P–T trajectory is related to emplacement time, depth, spatial location of the associated magma.

9.2. Late Archean high-pressure metamorphism

Late Archean metamorphic ages (2.50–2.45 Ga) were widely recognized in ~2.8–2.7 Ga TTG rocks in Jiaodong, Luxi and Wuchuan areas of the NCC (Dong et al., 2012a; Jahn et al., 2008; Wan et al., 2014). Compared with TTG rocks, meta-sedimentary rocks can better record the peak age of metamorphism, and can estimate the temperature and pressure conditions of peak stage at the same time (Foster and Parrish, 2003; Jiao et al., 2015). Monazite is abundant in metapelites and sensitive to amphibolite-facies and granulite-facies metamorphism, and therefore monazite has become one of the most extensive minerals for dating in metamorphic rocks (Parrish, 1990; Rubatto et al., 2013; Wang et al., 2015c).

In this study, SIMS monazite U–Pb dating results of the kyanite-garnet two feldspar gneiss (13XWL22) give an age of 2519 ± 1 Ma (Fig. 9a). Zircons from leucosome give a weighted average $^{207}Pb/^{206}Pb$ age of 2518 ± 10 Ma, similar to the monazite dating

Table 5
Whole rock $\delta^{18}O$ values of XWLBL metapelites from the Yinshan Block.

Sample ID	Rock type	$\delta^{18}O$ values
13XWL22	Ky-Grt two feldspar gneiss	12.4‰
14XWL36	Bt-Grt gneiss	10.8‰
14XWL37	Ky-Grt two feldspar gneiss	12.1‰
14XWL37-1	Ky-Grt two feldspar gneiss (dark layer)	11.5‰

Please cite this article in press as: Wang, D., Guo, J. Late Archean high-pressure pelitic granulites in the Yinshan Block, North China Craton. Precambrian Res. (2017), http://dx.doi.org/10.1016/j.precamres.2017.03.027

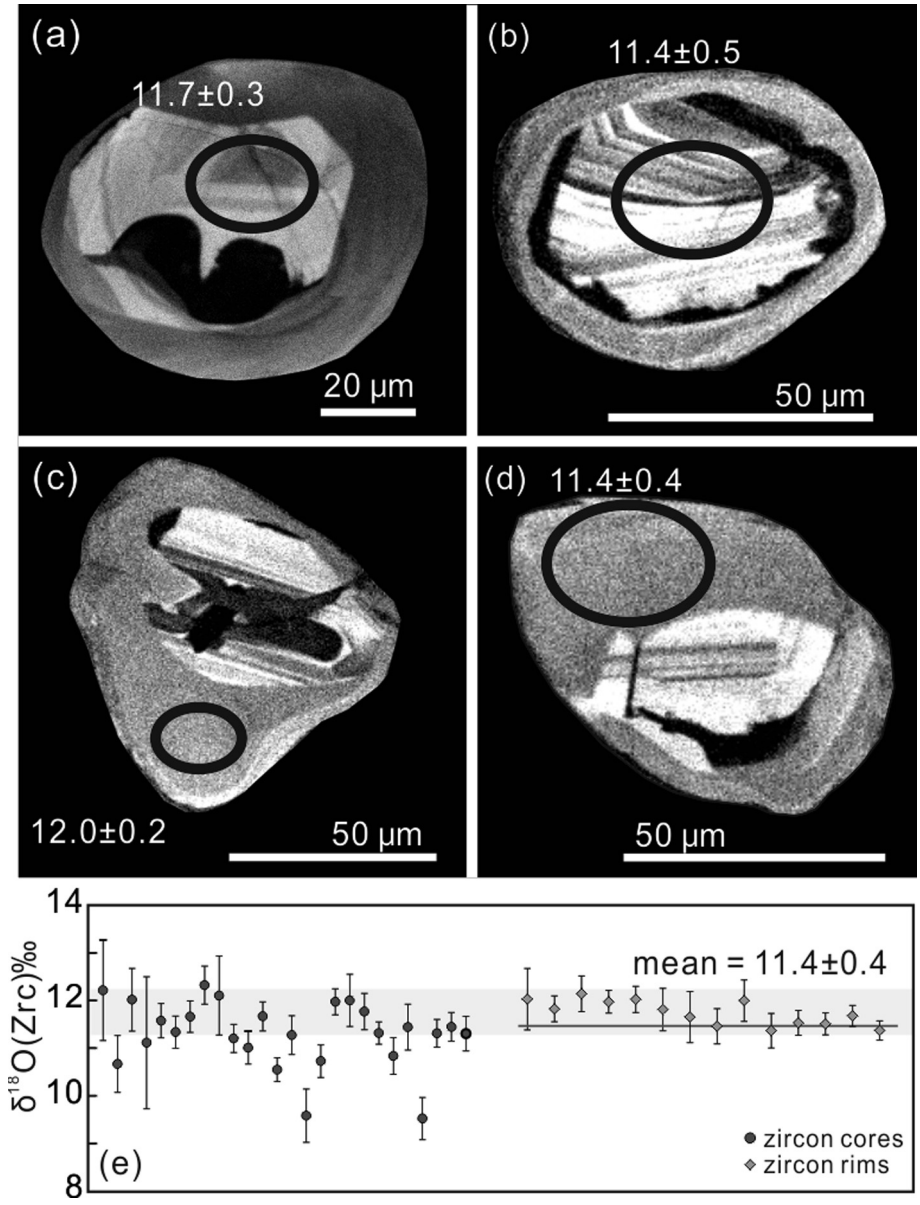

Fig. 10. (a–d) Representative CL images of analyzed zircons from metapelite (13XWL22) from the XWLBL area in the Yinshan Block; Black circles and numbers indicate zircon $\delta^{18}O$ analyzed positions and values, respectively. (e) Plots of zircon oxygen isotopes for detrital cores and metamorphic rims.

results. Thus, we consider that ~2.52 Ga represents the crystallization age of granulite-facies partial melt. Such an interpretation is supported by the homogeneous zoning pattern and narrow range of $^{207}Pb/^{206}Pb$ ages of monazite (Fig. 9a).

A lower intercept zircon age of ~1.8 ± 0.1 Ga was obtained from the leucosome (Fig. 9b), suggesting that zircon has lost lead due to a Paleoproterozoic thermal event that is related to the Paleoproterozoic subduction-collision in the Khondalite belt. However, Paleoproterozoic ages of monazites are absent in the metapelite. As monazite easily dissolves in melt-present conditions (Kelsey et al., 2008; Kohn et al., 2005) and may be partially reset by a secondary metamorphic overprint (Bhowmik et al., 2014; Cocherie et al., 1998), we suggest that the Paleoproterozoic high-grade metamorphism in the Khondalite belt has a weak effect on the Archean basement rocks in the Yinshan Block. Monazite ages younger than 2.49 Ga have not been obtained in this study, which indicates that multi-stage metamorphism around 2.50–2.45 Ga may not have occurred in the Yinshan Block (Dong et al., 2012a; Ma et al., 2013b; Zhang et al., 2014).

9.3. Nature of source

U–Pb ages of detrital zircon are potential indicators of sedimentary provenance (Andersen, 2005). Most detrital zircon cores from the kyanite-garnet two feldspar gneiss show clear oscillatory zoning (Fig. 10), suggesting a magmatic origin. These magmatic cores give apparent $^{207}Pb/^{206}Pb$ ages from 2576 Ma to 2733 Ma with a major peak at ~2610 Ma (Wang et al., 2015b), which reflects that the main source comes from the ~2.6 Ga magmatic rocks. ~2.7–2.6 Ga old meta-volcanics, TTG rocks and mafic-ultramafic plutons have been reported in the studied area (Dong et al., 2012a,b; Wang et al., 2015b) and may have been served as sediment source for the XWLBL metapelites.

Geochemical signature can also provide key information for sedimentary provenance. The XWLBL metapelites show high Na_2O (1.81–2.98 wt.%) contents but low K_2O contents (0.76–1.23 wt.%), different from Paleoproterzoic metamorphic sedimentary rocks from Hongshankou area in the Khondalite belt (Fig. 6c and d, Huang et al., 2016). In addition, the XWLBL

Please cite this article in press as: Wang, D., Guo, J. Late Archean high-pressure pelitic granulites in the Yinshan Block, North China Craton. Precambrian Res. (2017), http://dx.doi.org/10.1016/j.precamres.2017.03.027

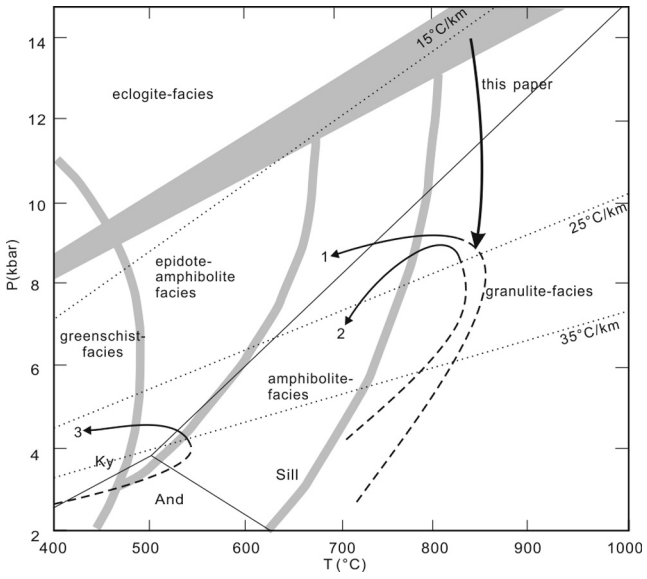

Fig. 11. Summary of the P–T conditions and paths for Archean high-grade metamorphic basement rocks in the Yinshan Block of the NCC. 1–mafic granulite from Wuchuan-Guyang area of the Western Block in the NCC (Lu and Xu, 1995); 2–mafic guanulite from Daqingshan area of the Western Block in the NCC (Jin et al., 1991); 3–Sheerteng group amphibolites (Jin, 1989). 1–3, details of above three P–T paths were summarized by Zhao et al. (1999). Alternate Al_2SiO_5 triple-point position is 501 °C/3.75 kbar by Holdaway and Mukhopadhyay (1993).

metapelites show high MgO (3.36–5.68 wt.%), Cr (245–421 ppm) and Ni (21.0–91.9 ppm) contents. Garnet shows high X_{prp} component in the metapelite (42–44%, Fig. 5b and e). Thus, the ~2.70–2.60 Ga old volcanic rocks are considered to be the main source of the pelites. Although TTG rocks have high Na_2O contents, they show low MgO, Cr and Ni contents and, therefore, are unlikely to be the source of sedimentary rocks. The XWLBL metapelites display weakly positive Eu anomaly in the chondrite-normalized diagram (Fig. 7a), indicating the presence of feldspar that crystallized from the melt during the granulite-facies metamorphism. It is also consistent with the field observation that near source leucosome is associated with the metapelites (Fig. 3a and b).

Oxygen isotopes of metapelites and zircons were used to investigate sedimentary processes. Zircon can preserve primary oxygen isotopic features even though underwent high-grade metamorphism (King et al., 1998). The XWLBL metapelites have high $\delta^{18}O$ (WR) values varying from 12.4‰ to 10.8‰, similar to the $\delta^{18}O$ values of the metamorphic zircons (mean = 11.43 ± 0.43‰, Fig. 10e). This suggests that the enrichment of oxygen isotope occurred before 2.5 Ga high-grade metamorphism. The reason of high oxygen isotopes in sedimentary rocks could be that they have undergone the low-temperature alteration in the surface. The peak pressure of kyanite-garnet gneiss defines at ~14–11 kbar (Fig. 8), suggesting that the lower crust has been thickened to a depth >40 km at ~2.52 Ga. The high $\delta^{18}O$ sedimentary rocks that brought into the lower crust could cause heterogeneous oxygen isotopes of the old Archean continental crust in the Yinshan Block.

9.4. Tectonic implications

HP granulites could either form in a subduction-collision setting, such as the Variscan Belt (Carswell and O'Brien, 1993), central-eastern Himalaya (Groppo et al., 2010; Liu and Zhong, 1997; Wang et al., 2016) and trans-North China Orogen of the NCC (e.g. Guo et al., 1996, 2002; Wei et al., 2001; Wu et al., 2014; Yin et al., 2014; Zhao et al., 1999), or in a deep arc environment that related to the extension or magmatic underplating (Appel and Schenk, 1998; Bohlen, 1987, 1991; Ellis, 1987; Müntener et al., 2000; Zhao and Zhai, 2013; Zhang et al., 2013). ~2.52 Ga clockwise P–T path HP pelitic granulites in the Yinshan Block (Fig. 8) were accompanied by large-scale coeval arc-related magmatic activities, i.e. high Mg-diorite, charnockite and TTG (Jian et al., 2012; Ma et al., 2013b; Zhang et al., 2014). Additionally, coeval anticlockwise P–T path of mafic rocks that are commonly observed in an arc environment were also identified in the studied areas (Fig. 11, Jin et al., 1991; Zhao et al., 1999). Taken together, we consider that the ~2.52 Ga HP granulites most likely formed in a continental arc environment.

In contrast, Paleoproterozoic HP metapelites in the Khondalite Belt were metamorphosed in a collision setting (Yin et al., 2014, 2015). Although Archean and Paleoproterozoic HP metapelites recorded similar metamorphic peak P–T conditions, they behaved differently during exhumation. The Paleoproterzoic metapelites underwent isothermally decompression from ~10 kbar to ~2–4 kbar, suggesting that they were rapidly brought to the middle-upper crust (Yin et al., 2014, 2015; Qiao et al., 2016); whereas the Archean metapelites isothermally decompressed from >11 kbar to ~8–10 kbar (deep crust) and then underwent prolonged cooling. Thus, the exhumation of HP granulites may provide information for discriminating an arc-root environment from a collision setting.

10. Conclusions

1) Phase equilibrium modelling results define the peak P–T conditions at >14–11 kbar and 840–870 °C, and a clockwise isothermal decompression P–T path.
2) SIMS monazite and zircon U–Pb dating of the kyanite-garnet metapelite and associated leucosome constrain the granulite-facies metamorphism at ~2519 Ma in the Yinshan Block of the NCC.
3) High Na_2O, MgO, Cr and Ni contents of the metapelites, combined with a peak age of ~2.60 Ga obtained from the detrital zircon cores, suggest that Neoarchean volcanics are the most likely source of the metapelites.
4) ~2.52 Ga magmatism and coeval HP pelitic granulites with clockwise P–T path supported a continental arc setting in the Yinshan Block of the NCC.

Acknowledgements

We are grateful to Fulai Liu and Guochun Zhao for their editorial handling and thoughtful suggestions. Chunming Wu and an anonymous are thanked for their constructive reviews. We thank Xianhua Li, Xiaoxiao Ling, Guoqiang Tang for their help with SIMS U–Pb dating and oxygen isotopes analysis, Lianjun Feng and Hongwei Li for their help with whole-rock oxygen isotopic analysis, and Qian Mao for assistance with electron microprobe analysis. Xudong Ma, Luojuan Wang, Guangyu Huang, Peng Liu and Dongjian Ouyang are thanked for their help in the field work. Discussion with Rolf L. Romer helped us to improve the manuscript. This study was supported by National Nature Science Foundation of China (Grant No. 41572174), the China Geological Survey (DD20160042) and China Postdoctoral Science Foundation (2016M601128). This is also contribution from the Sino-German (CSC–DAAD) Postdoc Scholarship Program of Dan Wang.

Appendix A

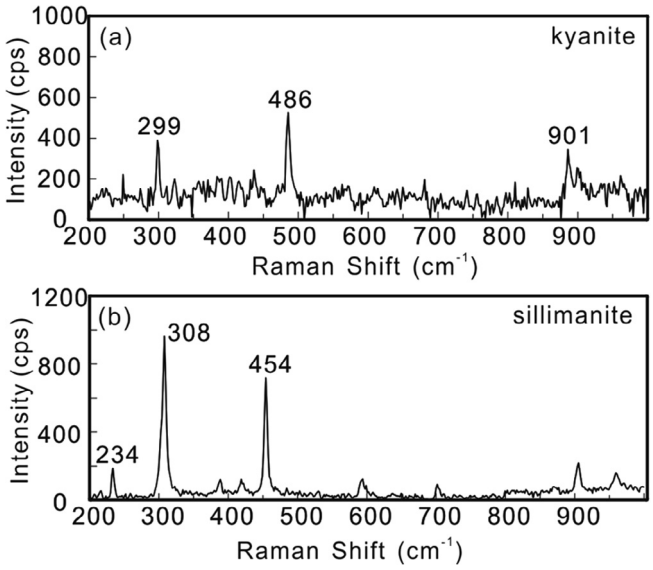

Fig. A. Appendix Laser Raman analysis to distinguish (a) kyanite and (b) sillimanite in the metapelite (13XWL22).

Table A
Appendix Major element compositions (wt.%) using in the phase equilibrium modelling for kyanite-garnet two feldspar gneiss (13XWL22) in the Yinshan Block (Fig. 8 and Appendix Fig. B).

Sample ID	14XWL22 XRF	Partial melts XRF	14XWL22 melt reintegrated
SiO_2	61.5	76.0	65.9
Al_2O_3	17.6	14.5	16.6
CaO	1.77	1.81	1.83
MgO	4.27	0.36	3.08
FeO	10.1	0.88	7.28
K_2O	0.78	1.61	1.03
Na_2O	3.06	4.77	3.58
MnO	0.11	0.01	0.08
TiO_2	0.79	0.13	0.59

For those metapelites that underwent melt loss, the XRF-based bulk composition can only be used to model the P–T conditions of melt crystallization or the retrograde evolution (Groppo et al., 2012). A 30 mol% melt, based on estimation of field outcrop, was reintegrated. Average of six XRF melt samples collected near the metapelites was used to calculate the melt-reintegrated bulk composition.
All Fe is presented as FeO. The major element contents are calculated on an H_2O-free basis, and chemical analyses are normalized to a total of 100%.

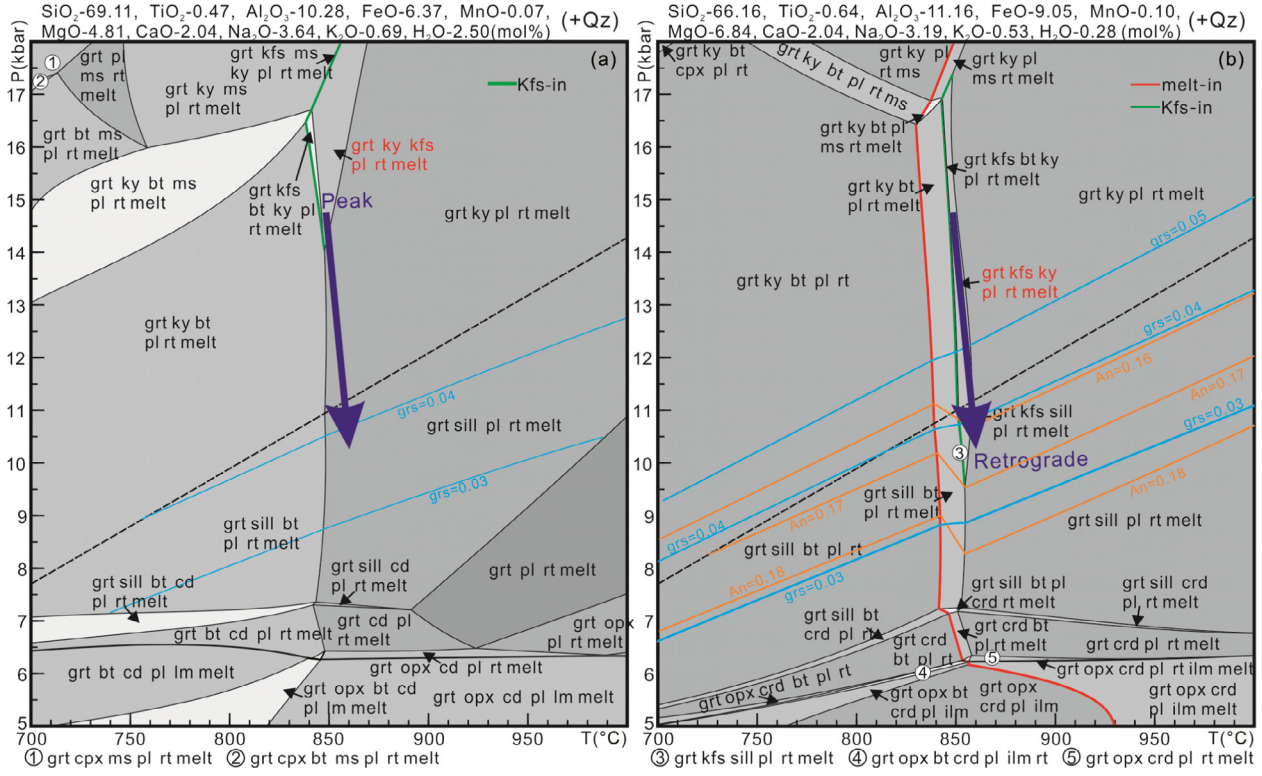

Fig. B. Appendix P–T Pesudosection calculated under MnNCKFMASHT system for kyanite-garnet two feldspar gneiss (Sample 13XWL22) at 5–18 kbar and 700–1000 °C, red characters represent peak mineral assemblage. (a) Pseudosection calculated using the melt-reintegrated bulk composition; (b) Pseudosection calculated using the XRF-based bulk composition.

Table B
Appendix SIMS monazite U–Pb isotopic data for the XWLBL kyanite-garnet two feldspar gneiss (13XWL22) in the Yinshan Block of the NCC.

Sample spot	$^{207}Pb/^{206}Pb$	±σ %	$^{207}Pb/^{235}U$	±σ %	$^{206}Pb/^{238}U$	±σ %	$^{207}Pb/^{206}Pb$	±σ	$^{207}Pb/^{235}U$	±σ	$^{206}Pb/^{238}U$	±σ	$^{206}Pb/^{204}Pb$ measured	f_{206}%	Th	U	Th/U
13XWL22@3	0.1633	0.11	10.60	1.50	0.4710	1.50	2490.6	1.9	2489	14	2488	31	2.99E+05	{0.05}	4.3	0.4	11.46
13XWL22@8	0.1645	0.24	10.77	1.53	0.4770	1.51	2502.6	4.0	2504	14	2514	31	6.70E+04	{0.18}	5.8	0.1	62.25
13XWL22@4	0.1653	0.23	10.80	1.54	0.4743	1.53	2510.4	3.8	2506	14	2502	32	2.71E+05	{0.03}	5.2	0.3	15.10
13XWL22@10	0.1658	0.20	11.04	1.53	0.4831	1.52	2515.3	3.4	2526	14	2541	32	2.44E+05	{0.03}	3.3	0.4	9.52
13XWL22@23	0.1658	0.15	10.94	1.51	0.4787	1.51	2515.6	2.5	2518	14	2521	31	1.58E+05	{0.03}	3.9	0.3	11.84
13XWL22@18	0.1660	0.14	11.01	1.51	0.4814	1.50	2517.5	2.3	2524	14	2534	32	2.40E+05	{0.01}	4.2	0.3	12.43
13XWL22@12	0.1660	0.19	10.91	1.53	0.4773	1.51	2517.8	3.2	2516	14	2515	32	2.03E+05	{0.03}	5.0	0.3	16.76
13XWL22@24	0.1660	0.32	10.88	1.54	0.4760	1.50	2517.9	5.4	2513	14	2510	31	9.61E+04	{0.02}	4.8	0.2	23.09
13XWL22@7	0.1661	0.14	10.91	1.51	0.4772	1.50	2518.4	2.4	2516	14	2515	31	1.89E+05	{0.03}	4.9	0.3	18.12
13XWL22@1	0.1661	0.12	10.82	1.51	0.4727	1.50	2518.8	1.9	2508	14	2495	31	4.00E+05	{0.14}	3.9	0.5	8.02
13XWL22@22	0.1662	0.14	10.88	1.51	0.4752	1.50	2519.4	2.4	2513	14	2506	31	1.79E+05	{0.02}	4.6	0.4	11.74
13XWL22@5	0.1662	0.12	11.01	1.51	0.4807	1.51	2519.7	2.1	2524	14	2530	32	2.36E+05	{0.02}	4.2	0.3	13.70
13XWL22@2	0.1663	0.15	11.09	1.51	0.4841	1.50	2520.6	2.5	2531	14	2545	32	3.69E+05	{0.02}	3.8	0.4	8.79
13XWL22@17	0.1663	0.17	10.99	1.52	0.4798	1.51	2520.7	2.9	2522	14	2526	32	2.83E+05	{0.02}	4.8	0.4	12.18
13XWL22@25	0.1663	0.27	10.92	1.52	0.4764	1.50	2520.7	4.6	2516	14	2511	31	1.75E+05	{0.03}	5.0	0.3	14.46
13XWL22@13	0.1663	0.19	11.08	1.52	0.4832	1.51	2520.8	3.1	2529	14	2541	32	2.47E+05	{0.04}	3.2	0.4	8.97
13XWL22@15	0.1663	0.12	11.07	1.57	0.4828	1.57	2521.0	2.0	2529	15	2539	33	4.58E+05	{0.02}	3.9	0.7	5.87
13XWL22@11	0.1664	0.11	10.97	1.54	0.4784	1.53	2521.9	1.9	2521	14	2520	32	2.99E+05	{0.02}	3.8	0.5	8.41
13XWL22@16	0.1666	0.16	10.90	1.52	0.4754	1.52	2523.8	2.7	2514	14	2507	32	1.48E+05	{0.07}	5.9	0.2	27.55
13XWL22@6	0.1666	0.15	10.88	1.52	0.4738	1.51	2524.3	2.6	2513	14	2500	31	3.21E+05	{0.02}	4.9	0.4	11.10
13XWL22@19	0.1667	0.10	10.91	1.51	0.4750	1.50	2524.4	1.6	2516	14	2506	31	3.96E+05	{0.02}	4.2	0.6	7.36
13XWL22@9	0.1667	0.43	10.88	1.56	0.4761	1.50	2524.6	7.2	2513	15	2510	31	4.19E+04	{0.03}	5.4	0.1	89.33
13XWL22@14	0.1668	0.21	10.94	1.53	0.4759	1.51	2525.9	3.5	2518	14	2510	32	2.29E+05	{0.03}	4.8	0.3	14.32
13XWL22@20	0.1671	0.18	10.78	1.51	0.4680	1.50	2528.9	3.1	2504	14	2475	31	2.79E+05	{0.03}	3.1	0.5	5.95
13XWL22@21	0.1674	0.12	10.83	1.51	0.4696	1.50	2531.7	2.0	2509	14	2482	31	2.44E+05	{0.06}	5.4	0.5	11.12

Table C
Appendix SIMS zircon U–Pb isotopic data for the XWLBL leucosome (14XWL35) in the Yinshan Block of the NCC.

Sample spot	$^{207}Pb/^{206}Pb$	±σ %	$^{207}Pb/^{235}U$	±σ %	$^{206}Pb/^{238}U$	±σ %	$^{207}Pb/^{206}Pb$	±σ	$^{207}Pb/^{235}U$	±σ	$^{206}Pb/^{238}U$	±σ	$^{206}Pb/^{204}Pb$ measured	f_{206}%	Th ppm	U ppm	Th/U
14XWL35@09	0.1181	0.32	5.420	1.54	0.3330	1.50	1926.9	5.8	1888.1	13.3	1853.0	24.2	1.05E+05	{0.02}	232	285	0.81
14XWL35@08	0.1276	0.51	6.275	1.60	0.3568	1.52	2064.6	9.0	2014.9	14.1	1966.9	25.8	1.43E+05	{0.01}	120	165	0.73
14XWL35@02	0.1341	1.28	7.165	2.90	0.3874	2.60	2152.8	22.1	2132.2	26.1	2110.9	46.9	5.53E+04	{0.03}	135	202	0.67
14XWL35@11	0.1358	1.02	6.936	1.82	0.3706	1.50	2173.8	17.6	2103.3	16.3	2032.0	26.3	7.86E+04	{0.02}	109	162	0.68
14XWL35@31	0.1406	1.64	7.505	2.32	0.3872	1.65	2234.1	28.0	2173.5	21.0	2110.0	29.7	1.58E+05	{0.01}	146	206	0.71
14XWL35@05	0.1429	0.91	7.849	1.92	0.3984	1.69	2262.5	15.6	2213.8	17.5	2161.7	31.2	2.33E+05	{0.01}	112	164	0.68
14XWL35@17	0.1456	0.72	8.258	1.74	0.4112	1.59	2295.4	12.4	2259.7	15.9	2220.4	29.9	5.86E+04	{0.03}	88	146	0.60
14XWL35@04	0.1458	0.42	8.333	1.58	0.4145	1.52	2297.2	7.3	2267.9	14.4	2235.6	28.8	1.30E+05	{0.01}	185	241	0.77
14XWL35@32	0.1540	1.63	9.926	2.23	0.4674	1.52	2391.3	27.5	2428.0	20.8	2472.0	31.2		{0.00}	118	169	0.70
14XWL35@15	0.1590	0.69	9.676	1.67	0.4415	1.52	2444.6	11.6	2404.4	15.5	2357.3	30.0	4.31E+04	{0.04}	116	170	0.68
14XWL35@37	0.1593	1.17	9.956	1.94	0.4533	1.54	2448.2	19.7	2430.7	18.0	2409.9	31.1	2.41E+05	{0.01}	220	267	0.83
14XWL35@23	0.1602	0.27	9.980	1.75	0.4518	1.73	2457.7	4.5	2432.9	16.3	2403.4	34.8	1.94E+05	{0.01}	236	273	0.87
14XWL35@41	0.1602	1.55	10.012	2.19	0.4532	1.54	2458.2	26.0	2435.9	20.4	2409.3	31.1	1.10E+05	{0.02}	121	183	0.66
14XWL35@12	0.1605	1.19	10.376	1.96	0.4690	1.55	2460.4	20.0	2468.9	18.3	2479.2	32.1	8.36E+04	{0.02}	111	158	0.70
14XWL35@06	0.1608	1.19	10.236	2.01	0.4616	1.62	2464.3	20.0	2456.3	18.7	2446.7	33.0	1.34E+05	{0.01}	132	188	0.70
14XWL35@24	0.1619	0.65	10.366	1.65	0.4643	1.52	2476.0	10.9	2468.0	15.4	2458.4	31.1	6.42E+05	{0.00}	195	219	0.89
14XWL35@10	0.1625	0.45	10.431	1.57	0.4656	1.50	2481.9	7.6	2473.8	14.7	2464.0	30.9	1.45E+05	{0.01}	137	202	0.68
14XWL35@16	0.1630	1.15	10.223	1.89	0.4549	1.50	2487.0	19.2	2455.2	17.6	2417.0	30.3	9.95E+04	{0.02}	155	213	0.73
14XWL35@18	0.1631	0.68	10.407	1.65	0.4628	1.50	2487.8	11.5	2471.7	15.4	2452.1	30.7	1.30E+05	{0.01}	140	217	0.65
14XWL35@25	0.1634	1.01	10.227	1.81	0.4540	1.51	2491.1	16.9	2455.6	16.9	2412.9	30.4	9.52E+05	{0.00}	98	154	0.64
14XWL35@20	0.1635	0.69	10.292	1.66	0.4566	1.51	2491.8	11.6	2461.4	15.5	2424.7	30.6	2.79E+04	{0.07}	352	335	1.05
14XWL35@19	0.1636	0.87	10.378	1.74	0.4600	1.50	2493.7	14.6	2469.1	16.2	2439.4	30.6	2.01E+05	{0.01}	116	173	0.67
14XWL35@39	0.1637	1.14	10.371	1.89	0.4594	1.50	2494.7	19.1	2468.5	17.6	2436.9	30.5	3.81E+05	{0.00}	122	183	0.67
14XWL35@07	0.1655	1.34	10.558	2.03	0.4626	1.52	2512.8	22.3	2485.0	19.0	2451.2	31.1	8.24E+04	{0.02}	108	182	0.59
14XWL35@13	0.1656	1.27	10.305	2.01	0.4513	1.55	2513.8	21.2	2462.5	18.7	2400.9	31.2	8.83E+03	{0.21}	126	204	0.62
14XWL35@14	0.1659	1.63	10.863	2.22	0.4750	1.51	2516.5	27.1	2511.5	20.9	2505.3	31.5	8.76E+04	{0.02}	102	166	0.61
14XWL35@22	0.1663	1.05	10.955	1.89	0.4779	1.57	2520.3	17.6	2519.3	17.8	2518.1	32.9	2.19E+05	{0.01}	135	192	0.71
14XWL35@01	0.1667	0.89	10.079	1.74	0.4384	1.50	2525.0	14.8	2442.0	16.2	2343.7	29.6	5.70E+03	{0.33}	133	192	0.69
14XWL35@29	0.1668	1.24	11.185	2.31	0.4864	1.95	2525.4	20.7	2538.7	21.7	2555.3	41.2	3.93E+05	{0.00}	376	320	1.17
14XWL35@36	0.1668	1.41	10.790	2.15	0.4693	1.63	2525.5	23.5	2505.2	20.2	2480.3	33.6	2.05E+05	{0.01}	110	170	0.65
14XWL35@38	0.1670	0.75	10.995	1.71	0.4775	1.54	2527.7	12.5	2522.7	16.1	2516.6	32.2		>1e6	108	161	0.67
14XWL35@21	0.1675	0.83	10.652	1.72	0.4614	1.50	2532.4	13.9	2493.3	16.1	2445.5	30.6	4.90E+04	{0.04}	401	373	1.07
14XWL35@03	0.1690	1.58	11.160	2.22	0.4789	1.55	2548.0	26.3	2536.5	20.9	2522.3	32.5	7.76E+04	{0.02}	168	219	0.76

Please cite this article in press as: Wang, D., Guo, J. Late Archean high-pressure pelitic granulites in the Yinshan Block, North China Craton. Precambrian Res. (2017), http://dx.doi.org/10.1016/j.precamres.2017.03.027

Table D
Appendix Zircon oxygen isotopic data of XWLBL kyanite-garnet two feldspar gneiss (13XWL22) in the Yinshan Block of the NCC.

Sample ID	Group	$\delta^{18}O$	2σ
13XWL22@2	Core	12.2	1.1
13XWL22@3	Core	10.7	0.6
13XWL22@4	Core	12.0	0.7
13XWL22@5	Core	11.1	1.4
13XWL22@8	Core	11.6	0.4
13XWL22@9	Core	11.3	0.3
13XWL22@10	Core	11.7	0.3
13XWL22@11	Core	12.3	0.4
13XWL22@12	Core	12.1	0.8
13XWL22@13	Core	11.2	0.3
13XWL22@14	Core	11.0	0.4
13XWL22@15	Core	11.7	0.3
13XWL22@17	Core	10.6	0.3
13XWL22@20	Core	11.3	0.4
13XWL22@22	Core	9.6	0.6
13XWL22@23	Core	10.7	0.3
13XWL22@24	Core	12.0	0.3
13XWL22@27	Core	12.0	0.6
13XWL22@30	Core	11.8	0.4
13XWL22@31	Core	11.3	0.2
13XWL22@32	Core	10.8	0.4
13XWL22@33	Core	11.4	0.5
13XWL22@34	Core	9.5	0.4
13XWL22@36	Core	11.3	0.3
13XWL22@37	Core	11.5	0.3
13XWL22@39	Core	11.3	0.4
13XWL22@1	Meta	12.0	0.6
13XWL22@6	Meta	11.8	0.3
13XWL22@7	Meta	12.2	0.4
13XWL22@16	Meta	12.0	0.2
13XWL22@18	Meta	12.0	0.3
13XWL22@19	Meta	11.8	0.5
13XWL22@21	Meta	11.7	0.5
13XWL22@25	Meta	11.5	0.4
13XWL22@26	Meta	12.0	0.4
13XWL22@28	Meta	11.4	0.4
13XWL22@29	Meta	11.5	0.3
13XWL22@35	Meta	11.5	0.2
13XWL22@38	Meta	11.7	0.2
13XWL22@40	Meta	11.4	0.2

References

Aleinikoff, J.N., Schenck, W.S., Plank, M.O., Srogi, L.A., Fanning, C.M., Kamo, S.L., Bosbyshell, H., 2006. Deciphering igneous and metamorphic events in high-grade rocks of the Wilmington Complex, Delaware: morphology, cathodoluminescence and backscattered electron zoning, and SHRIMP U-Pb geochronology of zircon and monazite. Geol. Soc. Am. Bull. 118, 39–64.

Andersen, T., 2005. Detrital zircons as tracers of sedimentary provenance: limiting conditions from statistics and numerical simulation. Chem. Geol. 216, 249–270.

Anderson, J.R., Payne, J.L., Kelsey, D.E., Hand, M., Collins, A.S., Santosh, M., 2012. High-pressure granulites at the dawn of the Proterozoic. Geology 40, 431–434.

Appel, P., Schenk, V., 1998. High-pressure granulite facies metamorphism in the Pan-African belt of eastern Tanzania: P-T–t evidence against granulite formation by continent collision. J. Metamorph. Geol. 16, 491–509.

Bhowmik, S.K., Wilde, S.A., Bhandari, A., Sarbadhikari, A.B., 2014. Zoned monazite and zircon as monitors for the thermal history of granulite terranes: an example from the Central Indian Tectonic Zone. J. Petrol. 55, 585–621.

Bohlen, S.R., 1987. Pressure-temperature-time paths and a tectonic model for the evolution of granulites. J. Geol., 617–632

Bohlen, S., 1991. On the formation of granulites. J. Metamorph. Geol. 9, 223–229.

Brown, M., 2006. Duality of thermal regimes is the distinctive characteristic of plate tectonics since the Neoarchean. Geology 34, 961.

Brown, M., 2007. Metamorphism, plate tectonics, and the supercontinent cycle. Earth Sci. Front. 14, 1–18.

Carswell, D., O'Brien, P., 1993. Thermobarometry and geotectonic significance of high-pressure granulites: examples from the Moldanubian Zone of the Bohemian Massif in Lower Austria. J. Petrol. 34, 427–459.

Chen, L., 2007. Geochronology and Geochemistry of the Guyang Greenstone Belt (Post-Doctorate Report). Institute of Geology and Geophysics, Chinese Academy of Sciences, Beijing, pp. 1–40 (in Chinese).

Cocherie, A., Legendre, O., Peucat, J., Kouamelan, A., 1998. Geochronology of polygenetic monazites constrained by in situ electron microprobe Th-U-total lead determination: implications for lead behaviour in monazite. Geochim. Cosmochim. Acta 62, 2475–2497.

Coggon, R., Holland, T.J.B., 2002. Mixing properties of phengitic micas and revised garnet-phengite thermobarometrys. J. Metamorph. Geol. 20, 683–696.

Condie, K.C., Kröner, A., 2008. When did plate tectonics begin? Evidence from the geologic record. Geol. Soc. Am. Spec. Pap. 440, 281–294.

Condie, K.C., Kröner, A., 2013. The building blocks of continental crust: evidence for a major change in the tectonic setting of continental growth at the end of the Archean. Gondwana Res. 23, 394–402.

Diener, J.F., Stevens, G., Kisters, A.F., Poujol, M., 2005. Metamorphism and exhumation of the basal parts of the Barberton greenstone belt, South Africa: constraining the rates of Mesoarchaean tectonism. Precambr. Res. 143, 87–112.

Diener, J., Stevens, G., Kisters, A., 2006. High-Pressure Intermediate-Temperature Metamorphism in the Southern Barberton Granitoid-Greenstone Terrain, South Africa: A Consequence of Subduction-Driven Overthickening and Collapse of Mid-Archean Continental Crust. Archean Geodynamics and Environments, pp. 239–254.

Dong, X.J., 2009. The Metamorphism Times and Tectonic Significance of High-grade Metamorphic Rocks in Xiwulangbulang Area Inner Mongolia [Master's thesis]. Jin-lin University, pp. 16–26 (in Chinese with English abstract).

Dong, C., Wan, Y., Xu, Z., Liu, D., Yang, Z., Ma, M., Xie, H., 2012a. SHRIMP zircon U-Pb dating of late Paleoproterozoic kondalites in the Daqing Mountains area on the North China Craton. Sci. China Earth Sci. 56, 115–125.

Dong, X., Xu, Z., Liu, Z., Sha, Q., 2012b. Zircon U-Pb geochronology of Archean high–grade metamorphic rocks from Xi Ulanbulang area, central Inner Mongolia. Sci. China Earth Sci. 55, 204–212.

Duan, Z., Wei, C., Qian, J., 2015. Metamorphic P-T paths and Zircon U–Pb age data for the Paleoproterozoic metabasic dykes of high-pressure granulite facies from Eastern Hebei, North China Craton. Precambr. Res. 271, 295–310.

Ellis, D., 1987. Origin and evolution of granulites in normal and thickened crusts. Geology 15, 167–170.

Foster, G., Parrish, R.R., 2003. Metamorphic monazite and the generation of P-T–t paths. Geol. Soc., London, Spec. Publ. 220, 25–47.

Geng, Y., Du, L., Ren, L., 2012. Growth and reworking of the early Precambrian continental crust in the North China Craton: constraints from zircon Hf isotopes. Gondwana Res. 21, 517–529.

Gong, W., Hu, J., Wu, S., Chen, H., Qu, H., Li, Z., Liu, Y., Wang, L., 2014. Possible south-westward extrusion of the Ordos Block in the Late Paleoproterozoic: constraints from kinematic and geochronologic analysis of peripheral ductile shear zones. Precambrian Res. 255, 716–733.

Groppo, C., Rubatto, D., Rolfo, F., Lombardo, B., 2010. Early oligocene partial melting in the main central thrust zone (Arun valley, eastern Nepal Himalaya). Lithos 118, 287–301.

Groppo, C., Rolfo, F., Indares, A., 2012. Partial melting in the Higher Himalayan Crystallines of Eastern Nepal: the effect of decompression and implications for the 'Channel Flow'model. J. Petrol. http://dx.doi.org/10.1093/petrology/egs009.

Guo, J.H., Bian, A.G., Shi, X., 1996. High-pressure granulite, retrograde eclogite and granite: early Precambrian Sangan Structure Zone. In: Zhai, M.G. (Ed.), Granulites and Lower Continental Crust in North China Archaean Craton. Seismological Press, Beijing, China, pp. 21–48.

Guo, J., Zhai, M., Xu, R., 2001. Timing of the granulite facies metamorphism in the Sanggan area, North China craton: zircon U-Pb geochronology. Sci. China, Ser. D Earth Sci. 44, 1010–1018.

Guo, J., O'Brien, P., Zhai, M., 2002. High-pressure granulites in the Sanggan area, North China craton: metamorphic evolution, P-T paths and geotectonic significance. J. Metamorph. Geol. 20, 741–756.

Guo, J.H., Sun, M., Chen, F.K., Zhai, M.G., 2005. Sm–Nd and SHRIMP U-Pb zircon geochronology of high-pressure granulites in the Sanggan area, North China Craton: timing of Paleoproterozoic continental collision. J. Asian Earth Sci. 24, 629–642.

Guo, J., Peng, P., Chen, Y., Jiao, S., Windley, B.F., 2012. UHT sapphirine granulite metamorphism at 1.93–1.92 Ga caused by gabbronorite intrusions: implications for tectonic evolution of the northern margin of the North China Craton. Precambr. Res. 222–223, 124–142.

Halpin, J.A., Clarke, G.L., White, R.W., Kelsey, D.E., 2007. Contrasting P-T–t paths for Neoproterozoic metamorphism in MacRobertson and Kemp Lands, east Antarctica. J. Metamorph. Geol. 25, 683–701.

Harley, S., 1989. The origins of granulites: a metamorphic perspective. Geol. Mag. 126, 215–247.

Holdaway, M.J., Mukhopadhyay, B., 1993. A reevaluation of the stability relations of andalusite: thermochemical data and phase diagram for the aluminum silicates. Am. Mineral. 78, 298–315.

Holland, T.J.B., Powell, R., 1998. An internally consistent thermodynamic dataset for phases of petrological interest. J. Metamorph. Geol. 16, 309–343.

Holland, T.J.B., Powell, R., 2003. Activity-composition relations for phases in petrological calculations: an asymmetric multicomponent formulation. Contrib. Miner. Petrol. 145, 492–501.

Hu, J., Gong, W., Wu, S., Liu, Y., Liu, S., 2014. LA–ICP–MS zircon U-Pb dating of the Langshan Group in the northeast margin of the Alxa block, with tectonic implications. Precambr. Res. 255, 756–770.

Huang, G., Jiao, S., Guo, J., Peng, P., Wang, D., Liu, P., 2016. P-T–t constraints of the Barrovian-type metamorphic series in the Khondalite belt of the North China Craton: evidence from phase equilibria modeling and zircon U–Pb geochronology. Precambr. Res. 283, 125–143.

Jahn, B., Zhou, X., Li, J., 1990. Formation and tectonic evolution of southeastern China and Taiwan: isotopic and geochemical constraints. Tectonophysics 183, 145–160.

Please cite this article in press as: Wang, D., Guo, J. Late Archean high-pressure pelitic granulites in the Yinshan Block, North China Craton. Precambrian Res. (2017), http://dx.doi.org/10.1016/j.precamres.2017.03.027

Jahn, B.M., Liu, D., Wan, Y., Song, B., Wu, J., 2008. Archean crustal evolution of the Jiaodong Peninsula, China, as revealed by zircon SHRIMP geochronology, elemental and Nd–isotope geochemistry. Am. J. Sci. 308, 232–269.

Jian, P., Zhang, Q., Liu, D.Y., Jin, W.J., Jia, X.Q., Qian, Q., 2005. SHRIMP dating and geological significance of Late Achaean high-Mg diorite (sanukite) andhornblende-granite at Guyang of Inner Monglia. Acta Petrol. Sin. 21, 151–157 (in Chinese with English abstract).

Jian, P., Kröner, A., Windley, B.F., Zhang, Q., Zhang, W., Zhang, L., 2012. Episodic mantle melting–crustal reworking in the late Neoarchean of the northwestern North China Craton: zircon ages of magmatic and metamorphic rocks from the Yinshan Block. Precambr. Res. 222–223, 230–254.

Jiao, S., Guo, J., Harley, S.L., Peng, P., 2013a. Geochronology and trace element geochemistry of zircon, monazite and garnet from the garnetite and/or associated other high-grade rocks: implications for Palaeoproterozoic tectonothermal evolution of the Khondalite Belt, North China Craton. Precambr. Res. 237, 78–100.

Jiao, S., Guo, J., Harley, S.L., Windley, B.F., 2013b. New constraints from garnetite on the P-T path of the Khondalite Belt: implications for the tectonic evolution of the North China Craton. J. Petrol. 54, 1725–1758.

Jiao, S.J., Guo, J.H., Wang, L.J., Peng, P., 2015. Short-lived high-temperature prograde and retrograde metamorphism in Shaerqin sapphirine-bearing metapelites from the Daqingshan terrane, North China Craton. Precambr. Res. 269, 31–57.

Jin, W., 1989. Metamorphic Evolution of the Archean to Palaeoproterozoic Basement Rocks in Daqingshan-Ulashan Area (in Chinese with English abstract) Unpublished Ph.D. thesis. Changchun University of Science and Technology, Changchun, p. 203.

Jin, W., Li, S.X., Liu, X.S., 1991. A study on characteristics of Early Precambrian high-grade metamorphic rock series and their metamorphic dynamics. Acta Petrol. Sin. 11, 27–35 (in Chinese with English abstract).

Kelsey, D., Clark, C., Hand, M., 2008. Thermobarometric modelling of zircon and monazite growth in melt-bearing systems: examples using model metapelitic and metapsammitic granulites. J. Metamorph. Geol. 26, 199–212.

King, E.M., Valley, J.W., Davis, D.W., Edwards, G.R., 1998. Oxygen isotope ratios of Archean plutonic zircons from granite–greenstone belts of the Superior Province: indicator of magmatic source. Precambr. Res. 92, 365–387.

Klemd, R., Bröcker, M., 1999. Fluid influence on mineral reactions in ultrahigh-pressure granulites: a case study in the Śnieżnik Mts. (West Sudetes, Poland). Contrib. Miner. Petrol. 136, 358–373.

Kohn, M., Wieland, M., Parkinson, C., Upreti, B., 2005. Five generations of monazite in Langtang gneisses: implications for chronology of the Himalayan metamorphic core. J. Metamorph. Geol. 23, 399–406.

Kryza, R., Pin, C., Vielzeuf, D., 1996. High-pressure granulites from the Sudetes (south-west Poland): evidence of crustal subduction and collisional thickening in the Variscan Belt. J. Metamorph. Geol. 14, 531–546.

Kusky, T.M., 2011. Geophysical and geological tests of tectonic models of the North China Craton. Gondwana Res. 20, 26–35.

Kusky, T.M., Li, J., 2003. Paleoproterozoic tectonic evolution of the North China Craton. J. Asian Earth Sci. 22, 383–397.

Kusky, T., Windley, B., Zhai, M.-G., 2007. Tectonic evolution of the North China Block: from orogen to craton to orogen. Geol. Soc., London, Spec. Publ. 280, 1–34.

Kusky, T.M., Polat, A., Windley, B.F., Burke, K.C., Dewey, J.F., Kidd, W.S.F., Maruyama, S., Wang, J.P., Deng, H., Wang, Z.S., Wang, C., Fu, D., Li, X.W., Peng, H.T., 2016. Insights into the tectonic evolution of the North China craton through comparative tectonic analysis: a record of outward growth of Precambrian continents. Earth Sci. Rev.

Li, X.H., Liu, Y., Li, Q.L., Guo, C.H., Chamberlain, K.R., 2009. Precise determination of Phanerozoic zircon Pb/Pb age by multicollector SIMS without external standardization. Geochem. Geophys. Geosyst. 10. http://dx.doi.org/10.1029/2009gc002400.

Li, X.H., Li, W.X., Li, Q.L., Wang, X.C., Liu, Y., Yang, Y.H., 2010a. Petrogenesis and tectonic significance of the similar to 850 Ma Gangbian alkaline complex in South China: evidence from in situ zircon U-Pb dating, Hf–O isotopes and whole-rock geochemistry. Lithos 114, 1–15.

Li, X.H., Long, W.G., Li, Q.L., Liu, Y., Zheng, Y.F., Yang, Y.H., Chamberlain, K.R., Wan, D. F., Guo, C.H., Wang, X.C., Tao, H., 2010b. Penglai zircon megacrysts: a potential new working reference material for microbeam determination of Hf–O isotopes and U-Pb age. Geostand. Geoanal. Res. 34, 117–134.

Li, Q.L., Li, X.H., Liu, Y., Tang, G.Q., Yang, J.H., Zhu, W.G., 2010c. Precise U-Pb and Pb–Pb dating of Phanerozoic baddeleyite by SIMS with oxygen flooding technique. J. Anal. At. Spectrom. 25, 1107–1113.

Li, X.P., Yang, Z., Zhao, G., Grapes, R., Guo, J., 2011. Geochronology of khondalite-series rocks of the Jining Complex: confirmation of depositional age and tectonometamorphic evolution of the North China craton. Int. Geol. Rev. 53, 1194–1211.

Li, Q.L., Li, X.H., Lan, Z.W., Guo, C.L., Yang, Y.N., Liu, Y., Tang, G.Q., 2013. Monazite and xenotime U-Th–Pb geochronology by ion microprobe: dating highly fractionated granites at Xihuashan tungsten mine, SE China. Contrib. Miner. Petrol. 166, 65–80.

Li, X., Zhang, L., Wei, C., Slabunov, A.I., 2015. Metamorphic PT path and zircon U-Pb dating of Archean eclogite association in Gridino complex, Belomorian province, Russia. Precambr. Res. 268, 74–96.

Liu, Y., Zhong, D., 1997. Petrology of high-pressure granulites from the eastern Himalayan syntaxis. J. Metamorph. Geol. 15, 451–466.

Liu, D., Nutman, A., Compston, W., Wu, J., Shen, Q.H., 1992. Remnants of ≥3800 Ma crust in the Chinese part of the Sino-Korean craton. Geology 20, 339–342.

Liu, X., Jin, W., Li, S., Xu, X., 1993. Two types of Precambrian high-grade metamorphism, Inner Mongolia, China. J. Metamorph. Geol. 11, 499–510.

Liu, S.W., Pan, Y.M., Xie, Q.L., Zhang, J., Li, Q.G., 2004. Archean geodynamics in the Central Zone, North China Craton: constraints from geochemistry of two contrasting series of granitoids in the Fuping and Wutai complexes. Precambr. Res. 130, 229–249.

Lu, L.Z., Jin, S.Q., 1993. P-T–t paths and tectonic history of an early Precambrian granulite facies terrane, Jining district, southeastern Inner Mongolia, China. J. Metamorph. Geol. 11, 483–498.

Lu, L., Xu, X., 1995. Metamorphism and deformation of metamorphic blocks in Yinshan-Northern Hebei Province. Metamorphic Dynamics and Deformation of the Early Precambrian Rocks in the North China Craton. Changchun University of Science & Technology, Changchun, pp. 75–90.

Lu, L.Z., Jin, S.Q., Xu, X.T., Liu, F.L., 1992. Petrogenesis and Mineralization of Khondalites in Southeastern Inner Mongolia. Jilin Science Technology Press, Changchun.

Ludwig, K., 2009. Isoplot v. 3.71: a geochronological Toolkit for Microsoft Excel: Berkeley. California. Berkeley Geochronol. Center Spec. Publ. 4, 70.

Ma, X., Fan, H.-R., Santosh, M., Guo, J., 2013a. Geochemistry and zircon U-Pb chronology of charnockites in the Yinshan Block, North China Craton: tectonic evolution involving Neoarchaean ridge subduction. Int. Geol. Rev. 55, 1688–1704.

Ma, X., Guo, J., Liu, F., Qian, Q., Fan, H., 2013b. Zircon U-Pb ages, trace elements and Nd–Hf isotopic geochemistry of Guyang sanukitoids and related rocks: implications for the Archean crustal evolution of the Yinshan Block, North China Craton. Precambr. Res. 230, 61–78.

Mahar, E.M., Baker, J.M., Powell, R., Holland, T.J.B., Howell, N., 1997. The effect of Mn on mineral stability in metapelites. J. Metamorph. Geol. 15, 223–238.

McDonough, W.F., Sun, S.S., 1995. The composition of the Earth. Chem. Geol. 120, 223–253.

Mints, M., Belousova, E., Konilov, A., Natapov, L., Shchipansky, A., Griffin, W., O'Reilly, S., Dokukina, K., Kaulina, T., 2010. Mesoarchean subduction processes: 2.87 Ga eclogites from the Kola Peninsula, Russia. Geology 38, 739–742.

Moyen, J.F., Stevens, G., Kisters, A., 2006. Record of mid-Archaean subduction from metamorphism in the Barberton terrain, South Africa. Nature 442, 559–562.

Müntener, O., Hermann, J., Trommsdorff, V., 2000. Cooling history and exhumation of lower-crustal granulite and upper mantle (Malenco, Eastern Central Alps). J. Petrol. 41, 175–200.

Nutman, A., 2001. On the scarcity of >3900 Ma detrital zircons in ≥3500 Ma metasediments. Precambr. Res. 105, 93–114.

O'Brien, E., Asmar, R., Beilin, L., Imai, Y., Mancia, G., Mengden, T., Myers, M., Padfield, P., Palatini, P., Parati, G., 2005. Practice guidelines of the European Society of Hypertension for clinic, ambulatory and self blood pressure measurement. J. Hypertens. 23, 697–701.

Parrish, R.R., 1990. U-Pb dating of monazite and its application to geological problems. Can. J. Earth Sci. 27, 1431–1450.

Peng, P., Guo, J.H., Windley, B.F., Li, X.H., 2011. Halaqin volcano-sedimentary succession in the central-northern margin of the North China Craton: products of late Paleoproterozoic ridge subduction. Precambr. Res. 187, 165–180.

Peng, P., Guo, J.H., Windley, B.F., Liu, F., Chu, Z., Zhai, M.G., 2012. Petrogenesis of Late Paleoproterozoic Liangcheng charnockites and S–type granites in the central-northern margin of the North China Craton: implications for ridge subduction. Precambr. Res. 222–223, 107–123.

Polat, A., Herzberg, C., Munker, C., Rodgers, R., Kusky, T., Li, J., Fryer, B., Delaney, J., 2006. Geochemical and petrological evidence for a suprasubduction zone origin of Neoarchean (ca. 2.5 Ga) peridotites, central orogenic belt, North China craton. Geol. Soc. Am. Bull. 118, 771–784.

Powell, R., Holland, T.J.B., 1988. An internally consistent thermodynamic dataset with uncertainties and correlations: application methods, worked examples and a computer program. J. Metamorph. Geol. 6, 173–204.

Powell, R., Holland, T.J.B., 1999. Relating formulations of the thermodynamics of mineral solid solutions: activity modelling of pyroxenes, amphiboles and micas. Am. Mineral. 84, 1–14.

Qiao, H., Yin, C., Li, Q., He, X., Qian, J., Li, W., 2016. Application of the revised Ti-in-zircon thermometer and SIMS zircon U-Pb dating of high-pressure pelitic granulites from the Qianlishan-Helanshan Complex of the Khondalite Belt, North China Craton. Precambr. Res. 276, 1–13.

Rubatto, D., Chakraborty, S., Dasgupta, S., 2013. Timescales of crustal melting in the Higher Himalayan Crystallines (Sikkim, Eastern Himalaya) inferred from trace element-constrained monazite and zircon chronology. Contrib. Miner. Petrol. 165, 349–372.

Santosh, M., 2010. Assembling North China Craton within the Columbia supercontinent: the role of double-sided subduction. Precambr. Res. 178, 149–167.

Schwandt, C.S., Cygan, R.T., Westrich, H.R., 1996. Ca self-diffusion in grossular garnet. Am. Mineral. 81, 448–451.

Song, B., Nutman, A.P., Liu, D., Wu, J., 1996. 3800 to 2500 Ma crustal evolution in the Anshan area of Liaoning Province, northeastern China. Precambr. Res. 78, 79–94.

Stacey, J.S., Kramers, J.D., 1975. Approximation of terrestrial lead isotope evolution by a two-stage model. Earth Planet. Sci. Lett. 26, 207–221.

Tang, Q., Li, C., Zhang, M., Ripley, E.M., Wang, Q., 2014. Detrital zircon constraint on the timing of amalgamation between Alxa and Ordos, with exploration implications for Jinchuan-type Ni–Cu ore deposit in China. Precambr. Res. 255, 748–755.

Please cite this article in press as: Wang, D., Guo, J. Late Archean high-pressure pelitic granulites in the Yinshan Block, North China Craton. Precambrian Res. (2017), http://dx.doi.org/10.1016/j.precamres.2017.03.027

Thompson, A.B., England, P.C., 1984. Pressure–temperature–time paths of regional metamorphism II. Their inference and interpretation using mineral assemblages in metamorphic rocks. J. Petrol. 25, 929–955.
Tong, L., Liu, X., Wang, Y., Liang, X., 2014. Metamorphic P-T paths of metapelitic granulites from the Larsemann Hills. East Antarctica. Lithos 192, 102–115.
Wan, Y., Liu, D., Song, B., Wu, J., Yang, C., Zhang, Z., Geng, Y., 2005. Geochemical and Nd isotopic compositions of 3.8 Ga meta-quartz dioritic and trondhjemitic rocks from the Anshan area and their geological significance. J. Asian Earth Sci. 24, 563–575.
Wan, Y., Song, B., Liu, D., Wilde, S.A., Wu, J., Shi, Y., Yin, X., Zhou, H., 2006. SHRIMP U-Pb zircon geochronology of Palaeoproterozoic metasedimentary rocks in the North China Craton: evidence for a major Late Palaeoproterozoic tectonothermal event. Precambr. Res. 149, 249–271.
Wan, Y., Liu, D., Dong, C., Xu, Z., Wang, Z., Wilde, S.A., Yang, Y., Liu, Z., Zhou, H., 2009. The Precambrian Khondalite Belt in the Daqingshan area, North China Craton: evidence for multiple metamorphic events in the Palaeoproterozoic era. Geol. Soc., London, Spec. Publ. 323, 73–97.
Wan, Y., Liu, D., Wang, S., Yang, E., Wang, W., Dong, C., Zhou, H., Du, L., Yang, Y., Diwu, C., 2011. ~2.7Ga juvenile crust formation in the North China Craton (Taishan-Xintai area, western Shandong Province): further evidence of an understated event from U-Pb dating and Hf isotopic composition of zircon. Precambr. Res. 186, 169–180.
Wan, Y., Xie, H., Yang, H., Wang, Z., Liu, D., Kroner, A., Wilde, S.A., Geng, Y., Sun, L., Ma, M., Liu, S., Dong, C., Du, L., 2013. Is the Ordos Block Archean or Paleoproterozoic in age? Implications for the Precambrian evolution of the North China Craton. Am. J. Sci. 313, 683–711.
Wan, Y., Xie, S., Yang, C., Kröner, A., Ma, M., Dong, C., Du, L., Xie, H., Liu, D., 2014. Early Neoarchean (~2.7 Ga) tectono-thermal events in the North China Craton: A synthesis. Precambr. Res. 247, 45–63.
Wang, F., Li, X.-P., Chu, H., Zhao, G., 2011. Petrology and metamorphism of khondalites from the Jining complex, North China craton. Int. Geol. Rev. 53, 212–229.
Wang, J., Kusky, T., Polat, A., Wang, L., Deng, H., Wang, S., 2013. A late Archean tectonic mélange in the Central Orogenic Belt, North China Craton. Tectonophysics 608, 929–946.
Wang, Y.-F., Li, X.-H., Jin, W., Zhang, J.-H., 2015a. Eoarchean ultra-depleted mantle domains inferred from ca. 3.81Ga Anshan trondhjemitic gneisses. North China Craton. Precambrian Research 263, 88–107.
Wang, D., Guo, J., Huang, G., Scheltens, M., 2015b. The Neoarchean ultramafic–mafic complex in the Yinshan Block, North China Craton: magmatic monitor of development of Archean lithospheric mantle. Precambr. Res. 270, 80–99.
Wang, J.-M., Rubatto, D., Zhang, J.-J., 2015c. Timing of partial melting and cooling across the Greater Himalayan crystalline complex (Nyalam, Central Himalaya): in-sequence thrusting and its implications. J. Petrol. 56, 1677–1702.
Wang, J.-M., Zhang, J.-J., Liu, K., Zhang, B., Wang, X.-X., Rai, S.M., Scheltens, M., 2016. Spatial and temporal evolution of tectonometamorphic discontinuities in the central Himalaya: constraints from P-T paths and geochronology. Tectonophysics 679, 41–60. http://dx.doi.org/10.1016/j.tecto.2016.04.035.
Wei, C.J., Zhang, C.G., Zhang, A.L., Wu, T.H., Li, J.H., 2001. Metamorphic P-T conditions and geological significance of high-pressure granulite from the Jianping complex, western Liaoning province. Acta Petrol. Sin. 17, 269–282.
Wei, C., Qian, J., Zhou, X., 2014. Paleoproterozoic crustal evolution of the Hengshan–Wutai–Fuping region, North China Craton. Geosci. Front. 5, 485–497.
White, R.W., Powell, R., Holland, T.J.B., Worley, B.A., 2000. The effect of TiO_2 and Fe_2O_3 on metapelitic assemblages at greenschist and amphibolite facies conditions: mineral equilibria calculations in the system K_2O–FeO–MgO–Al_2O_3–SiO_2–H_2O–TiO_2–Fe_2O_3. J. Metamorph. Geol. 18, 497–511.
White, R.W., Pomroy, N.E., Powell, R., 2005. An in-situ metatexite-diatexite transition in upper amphibolite facies rocks from Broken Hill, Australia. J. Metamorph. Geol. 23, 579–602.
White, R.W., Powell, R., Holland, T.J.B., 2007. Progress relating to calculation of partial melting equilibria for metapelites. J. Metamorph. Geol. 25, 511–527.
Williams, I.S., 1998. U-Th-Pb geochronology by ion microprobe. In: McKibben, Shanks, W.C., III, Ridley, W.I. (Eds.), Applications of microanalytical techniques to understanding mineralizing process. Reviews in economic geology, Vol. 7. Society of Economic Geologists, El Paso, p. 1.
Wu, F., Zhao, G., Wilde, S.A., Sun, D., 2005. Nd isotopic constraints on crustal formation in the North China Craton. J. Asian Earth Sci. 24, 523–545.
Wu, C.M., Lu, J.S., Wang, G.D., 2014. Determination of pressure–temperature conditions of retrograde symplectic assemblages in granulites and amphibolites. Glob. J. Earth Sci. Eng. 1, 71–83.
Xia, X.P., Sun, M., Zhao, G.C., Luo, Y., 2006a. LA–ICP–MS U-Pb geochronology of detrital zircons from the Jining Complex, North China Craton and its tectonic significance. Precambrian Res. 144, 199–212.
Xia, X., Sun, M., Zhao, G., Wu, F., Xu, P., Zhang, J., Luo, Y., 2006b. U-Pb and Hf isotopic study of detrital zircons from the Wulashan khondalites: constraints on the evolution of the Ordos Terrane, western block of the North China Craton. Earth Planet. Sci. Lett. 241, 581–593.
Xu, Z., Liu, Z., Dong, X., Dong, C., Wan, Y., 2011. Discovery of kyanite garnet quartz feldspathic gneiss in the north side of Daqing Mts., Inner Mongolia, and its petrography, geochemistry and zircon SHRIMP dating. Geol. Rev. 57, 243–252 (in Chinese with English abstract).
Yin, C., Zhao, G., Sun, M., Xia, X., Wei, C., Zhou, X., Leung, W., 2009. LA–ICP–MS U-Pb zircon ages of the Qianlishan Complex: constrains on the evolution of the Khondalite Belt in the Western Block of the North China Craton. Precambr. Res. 174, 78–94.
Yin, C., Zhao, G., Guo, J., Sun, M., Xia, X., Zhou, X., Liu, C., 2011. U-Pb and Hf isotopic study of zircons of the Helanshan Complex: constrains on the evolution of the Khondalite Belt in the Western Block of the North China Craton. Lithos 122, 25–38.
Yin, C., Zhao, G., Wei, C., Sun, M., Guo, J., Zhou, X., 2014. Metamorphism and partial melting of high-pressure pelitic granulites from the Qianlishan Complex: constraints on the tectonic evolution of the Khondalite Belt in the North China Craton. Precambr. Res. 242, 172–186.
Yin, C., Zhao, G., Sun, M., 2015. High-pressure pelitic granulites from the Helanshan Complex in the Khondalite Belt, North China Craton: metamorphic Pt path and tectonic implications. Am. J. Sci. 315, 846–879.
Zhai, M., 2011. Cratonization and the Ancient North China Continent: A summary and review. Sci. China Earth Sci. 54, 1110–1120.
Zhai, M., 2014. Multi-stage crustal growth and cratonization of the North China Craton. Geosci. Front. 5, 457–469.
Zhai, M.G., Santosh, M., 2011. The early Precambrian odyssey of the North China Craton: A synoptic overview. Gondwana Res. 20, 6–25.
Zhai, M., Santosh, M., 2013. Metallogeny of the North China Craton: link with secular changes in the evolving Earth. Gondwana Res. 24, 275–297.
Zhai, M., Bian, A., Zhao, T., 2000. The amalgamation of the supercontinent of North China Craton at the end of Neo-Archaean and its breakup during late Palaeoproterozoic and Meso-Proterozoic. Sci. China, Ser. D Earth Sci. 43, 219–232.
Zhai, M., Xiao, W., Kusky, T., Santosh, M., 2007. Tectonic evolution of China and adjacent crustal fragments. Gondwana Res. 12, 1–3.
Zhai, M., Li, T.-S., Peng, P., Hu, B., Liu, F., Zhang, Y., 2010. Precambrian key tectonic events and evolution of the North China Craton. Geol. Soc., London, Spec. Publ. 338, 235–262.
Zhang, Z., Dong, X., Xiang, H., Liou, J.G., Santosh, M., 2013. Building of the Deep Gangdese Arc, South Tibet: paleocene plutonism and Granulite-facies metamorphism. J. Petrol. 54, 2547–2580.
Zhang, X., Yuan, L., Xue, F., Zhai, M., 2014. Neoarchean metagabbro and charnockite in the Yinshan block, western North China Craton: petrogenesis and tectonic implications. Precambr. Res. 255, 563–582.
Zhang, C., Diwu, C., Kröner, A., Sun, Y., Luo, J., Li, Q., Gou, L., Lin, H., Wei, X., Zhao, J., 2015. Archean-Paleoproterozoic crustal evolution of the Ordos Block in the North China Craton: constraints from zircon U-Pb geochronology and Hf isotopes for gneissic granitoids of the basement. Precambr. Res. 267, 121–136.
Zhao, G., Zhai, M., 2013. Lithotectonic elements of Precambrian basement in the North China Craton: review and tectonic implications. Gondwana Res. 23, 1207–1240.
Zhao, G., Wilde, S.A., Cawood, P.A., Lu, L., 1998. Thermal evolution of Archean basement rocks from the eastern part of the North China Craton and its bearing on tectonic setting. Int. Geol. Rev. 40, 706–721.
Zhao, G., Wilde, S.A., Cawood, P.A., Lu, L., 1999. Tectonothermal history of the basement rocks in the western zone of the North China Craton and its tectonic implications. Tectonophysics 310, 37–53.
Zhao, G., Wilde, S.A., Cawood, P.A., Lu, L., 2000. Petrology and P-T path of the Fuping mafic granulites: implications for tectonic evolution of the central zone of the North China Craton. J. Metamorph. Geol. 18, 375–391.
Zhao, G., Wilde, S.A., Cawood, P.A., Sun, M., 2001. Archean blocks and their boundaries in the North China Craton: lithological, geochemical, structural and P-T path constraints and tectonic evolution. Precambr. Res. 107, 45–73.
Zhao, G., Wilde, S.A., Cawood, P.A., Sun, M., 2002. SHRIMP U-Pb zircon ages of the Fuping Complex: implications for late Archean to Paleoproterozoic accretion and assembly of the North China Craton. Am. J. Sci. 302, 191–226.
Zhao, G., Sun, M., Wilde, S.A., Sanzhong, L., 2005. Late Archean to Paleoproterozoic evolution of the North China Craton: key issues revisited. Precambr. Res. 136, 177–202.
Zhao, G., Wilde, S.A., Li, S., Sun, M., Grant, M.L., Li, X., 2007. U-Pb zircon age constraints on the Dongwanzi ultramafic–mafic body, North China, confirm it is not an Archean ophiolite. Earth Planet. Sci. Lett. 255, 85–93.
Zhao, G., Wilde, S.A., Sun, M., Li, S., Li, X., Zhang, J., 2008. SHRIMP U-Pb zircon ages of granitoid rocks in the Lüliang Complex: implications for the accretion and evolution of the Trans-North China Orogen. Precambr. Res. 160, 213–226.
Zhao, G., Wilde, S.A., Cawood, P.A., Lu, L., 2010. Thermal Evolution of Archean Basement Rocks from the Eastern Part of the North China Craton and Its Bearing on Tectonic Setting. Int. Geol. Rev. 40, 706–721.
Zhao, G., Cawood, P.A., Li, S., Wilde, S.A., Sun, M., Zhang, J., He, Y., Yin, C., 2012. Amalgamation of the North China Craton: key issues and discussion. Precambr. Res. 222, 55–76.

Please cite this article in press as: Wang, D., Guo, J. Late Archean high-pressure pelitic granulites in the Yinshan Block, North China Craton. Precambrian Res. (2017), http://dx.doi.org/10.1016/j.precamres.2017.03.027